Effect of the Processing Route on the Localized Corrosion Susceptibility of Al Alloy AA7050 in Saline Solutions

Effect of the Processing Route on the Localized Corrosion Susceptibility of Al Alloy AA7050 in Saline Solutions

By DARREN FEENSTRA, B.ENG.

A Thesis

Submitted to the Department of Materials Science & Engineering
and the School of Graduate Studies
in Partial Fulfilment of the Requirements
for the Degree
Master of Applied Science

McMaster University

McMaster University MASTER OF APPLIED SCIENCE (2016)
Hamilton, Ontario (Materials Science and Engineering)

TITLE: Effect of the Processing Route on the Localized Corrosion Susceptibility of Al Alloy AA7050 in Saline Solutions

AUTHOR: Darren R. Feenstra, B. Eng. (McMaster University)
SUPERVISOR: Dr. J.R. Kish
NUMBER OF PAGES: 136

Abstract

Experiments were conducted to characterize and compare the localized corrosion susceptibility of the granular microstructure of aluminum (Al) alloy AA7050 in the peak aged T6 condition cast by the novel controlled diffusion solidification (CDS) process against the conventional wrought plate counterpart. CDS is a casting technique that involves mixing two precursor melts at specific temperatures and compositions before solidification. This process avoids the problem of hot tearing by causing copious nucleation of the solid phase within the melt before solidification, reducing the amount of solute segregation and, thus dendritic growth creating a consistently equiaxed microstructure.

The effect of the CDS processing route on its relative localized corrosion susceptibility was elucidated by making links between the microstructure heterogeneities and the localized corrosion susceptibility as evaluated in aqueous saline solutions. Microstructures were characterized and compared with the use of the following techniques:

I. Scanning electron microscopy (SEM) to characterize grain size, shape and distribution.
II. Electron backscattered diffraction (EBSD) in SEM mode to characterize grain misorientation and the associated distribution.

III. Auger electron spectroscopy (AES) to characterize the composition of the grain boundary region including the precipitate free zone (PFZ) and the grain boundary precipitates.

IV. Atom probe tomography (APT) to define the size, distribution, and composition of the strengthening matrix precipitates along with the grain boundary region (PFZ and grain boundary precipitates).

Electrochemical experiments were conducted to characterize and compare the localized corrosion susceptibility of the two materials (CDS and conventional wrought) exhibited in aqueous saline solutions. Specific techniques include the following:

I. Potentiodynamic polarization measurements of mechanically-abraded surfaces to determine the corrosion potential (E_{corr}) and breakdown potential (E_b).

II. Potentiostatic anodic polarization of mechanically-abraded surfaces to observe the mode and extent of localized corrosion.

III. Open-circuit potential (OCP) measurements of fracture surfaces to determine the OCP of a surface with a significantly higher grain boundary area fraction relative to the bulk material.

IV. Cyclic acidified salt (sodium chloride (NaCl)) fog testing (ASTM-G85-Annex 2) to validate the relative localized corrosion susceptibility under more realistic atmospheric corrosion exposure conductions.

The CDS casting technique resulted in an entirely equiaxed microstructure. The microstructure was isotropic with an average grain size of $25 \pm 1\ \mu\mathrm{m}$ and an aspect ratio of around 1. This grain structure was in stark contrast with the wrought material, which exhibited a granular structure elongated along the rolling direction. The wrought material had a cord length of $56 \pm 3.2\ \mu\mathrm{m}$ in the rolling direction, $51 \pm 3\ \mu\mathrm{m}$ in the traverse direction and $13.3 \pm 1.6\ \mu\mathrm{m}$ in the short traverse direction. The wrought material had an aspect ratio of around 4 in the longitudinal plane (LS), 2.6 in the short transverse plane (ST) and 1.2 in the rolling plane (LT). AES and APT revealed that the CDS material had a higher amount of copper (Cu) segregation into the grain boundary precipitates. Electrochemical testing showed that the wrought material had a E_b of −750 ± 3 mV while the CDS had a higher E_b of −697 ± 4 mV. The Cu segregation into the grain boundary precipitates yielded more electrochemically active grain boundaries, as revealed by the OCP measurements. Despite this fact, localized corrosion of the CDS material initiated as pitting and propagated as a mixed mode involving intergranular corrosion (IGC) and pitting. The localized corrosion mode

exhibited by the wrought material was purely IGC: both in initiation and propagation. The difference in corrosion mode was found to be due to the differences in the size of the Fe-based IMPs and the distribution of the Cu secondary phase precipitates: The CDS had large Fe IMP trapped at the grain boundary triple points and clustering of Cu secondary phase precipitates. Conversely, the wrought material had finely dispersed Fe IMP of significantly smaller size than those found in the CDS, and its Cu secondary phase precipitates are evenly distributed along the grain boundaries. These differences in precipitate distribution enhanced susceptibility for pitting in the CDS and reduced the driving force for IGC. The propagation of localized corrosion was markedly reduced in the CDS material: about half of that exhibited by the wrought material (under identical exposure conditions). Cyclic acidified salt fog testing revealed industry acceptable levels of localized corrosion susceptibility in-line with the benchmark alloys that are currently used in automotive applications.

Acknowledgements

My deepest gratitude goes first to my supervisor Dr. Joesph Kish: for his ever-present guidance and encouragement. He has been directly involved in my development as a researcher and professional and I am extremely thankful for his selfless promotion of both my portfolio and career as an engineer. For his consistent approach as teacher and mentor, I cannot thank him enough. Without his efforts, this project and thesis would not be possible.

I would also like to acknowledge my fellow colleagues in the Department of Materials Science and Engineering at McMaster University as well as those in my research group at the Centre for Automotive Materials and Corrosion, for their willingness in sharing their knowledge, sacrifice of time and providing insight into my work, I am incredibly grateful.

The following individuals deserve recognition for their particular impact on my project: Dr. Joseph McDermid for his constant presence in motivation and professional opinion. Dr. Elizabeth McNally for her role in my tenure as a mentor. Dr. Brian Langelier for his expertise and analysis in Atom Probe Tomography, Shooka Mahboubi for her assistance in my Auger Microscopy work.

My precious parents James and Cathy along with my family, who have stood by me through this project. For their patience during my frustration, encouragement during my angst, celebration in my victories, I am eternally grateful.

Lastly, I dedicated this work to my Lord and Saviour Jesus Christ. He is the only source of true meaning and purpose in my life. He has overfilled my cup with blessings beyond count. All my work is to the glory of His name. Praise God from whom all blessings flow.

Abbreviations and Symbols

List of Abbreviations

AA	Aluminum Association
AR	As-Received
APT	Atom Probe Tomography
CDS	Controlled Diffusion Solidification
CS	Cross Section
EBSD	Electron Backscatter Diffraction
EDS	Energy Dispersive X-Ray Spectroscopy
FIB	Focused Ion Beam
GDOES	Glow Discharge Optical Electron Spectroscopy
GPZ	Guinier-Preston Zones
HAGB	High Angle Grain Boundary
IGC	Intergranular Corrosion
IMP	Intermetallic Particle
L	Longitudinal (rolling) Direction
LOM	Light Optical Microscopy
LAGB	Low Angle Grain Boundary
MAGB	Medium Angle Grain Boundary
OCP	Open Circuit Potential
OPS	water-free silica colloidal Oxide Polishing Suspension
PFZ	Precipitate Free Zone

RT	Room Temperature
S	Short Transverse Direction
SEM	Scanning Electron Microscopy
SCC	Stress Corrosion Cracking
SCE	Standard Calomel Electrode
T	Transverse Direction

List of Symbols

A	Ampere
m	Metre
˚C	Degrees Celsius
E_b	Breakdown Potential
E_{corr}	Corrosion Potential
E_{OCP}	Open Circuit Potential
eV	Electron Volt
g	Gram
h	Hour
I	Current, A
i	Current Density, mA/cm^2
i_{corr}	Corrosion Current Density mA/cm^2
J	Joule
M	Molarity, moles/L
min	Minutes
L	Litre
mV/s	Millivolt per second
s	Seconds
V	Volt
wt %	Weight Percent

Table of Contents

Chapter 4: Experimental Methods 35

Chapter 5: Results 50

List of Tables

List of Figures

Chapter 1: Introduction

Present economic and political influences have resulted in an increased focus of research in the field of automotive lightweighting for the purpose of fuel consumption reduction. Many researchers are exploring light metal alloys such as magnesium (Mg) and aluminum (Al) as the solution to reducing passenger vehicle weight. Over the past 15 years, the use of Al alloys in passenger vehicles has accelerated. Currently, the highest volume of Al components in cars is in castings such as engine blocks, cylinder heads, and chassis [1]. Application though is limited where certain components have high requirements on strength and durability.

Aluminum Association (AA) 7xxx (Al-Zn-Mg-Cu) and 2xxx (Al-Cu-Mg) series alloys are used in structural automotive and aerospace due to their high strength to weight ratio and good ductility. Unfortunately utilization of AA7xxx alloys is restricted to the wrought form since the casting form is prone to hot tearing caused by primarily significant solute segregation, large primary Al grains and dendritic structure [2]. Controlled Diffusion Solidification (CDS) is a new casting technique that has been developed to address the problem of hot tearing. CDS involves mixing two precursor-melts at specific temperatures and compositions before solidification. This process avoids hot tearing by causing copious nucleation in the melt before solidification. This nucleation event greatly reduces the amount of solute segregation and dendritic growth resulting in a consistently equiaxed microstructure in the casting: potentially allowing the application of thin wall AA7xxx alloy castings such as automotive structural components.

The addition of Cu to AA7xxx alloys significantly increases the mechanical properties through precipitation hardening [3]; precipitation hardening is possible in Al-Zn-Mg alloys due to the limited solubility of Mg and Zn in the α phase. The generally accepted precipitate sequence that Al-Zn-Mg alloys undergo is super saturated solid solution (SSSS) → GP zones (I, II) → η′(coherent) → η (incoherent). An AA7xxx is first solutionized as it is heated above the solvus temperature and homogenized to produce a solid solution of α. As the material is quickly quenched the solubility of Mg and Zn decreases without allowing time for diffusion. Aging is then completed by heating at a low temperature to allow short-range diffusion to produce small finely dispersed η incoherent $MgZn_2$ precipitates. The addition of over 1% Cu has been shown to accelerate the precipitation kinetics of GP zones to the η′ phase and stabilize the η′ phase preventing it from changing into the η phase. The η′ phase provides the most strength in the Al-Mg-Zn alloy by limit dislocation mobility [3]. Unfortunately with the addition of Cu, the peak-aged T6 heat treatment that provides the maximum strength also results in an increased susceptibility to localized corrosion modes, including pitting, crevice, intergranular and exfoliation, in chloride-containing environments.

AA7050-T6 has a heterogeneous microstructure consisting of an Al matrix, coarse intermetallic particles (IMPs), fine strengthening matrix precipitates, PFZs adjacent to grain boundaries and grain boundary precipitates. Cu is distributed throughout the microstructure in several forms: (i) within $Mg(Zn,Cu,Al)_2$ precipitates and its derivatives on the nanometer scale, which account for most of Cu in the alloy, (ii) coarse IMPs such as Al_2CuMg (S phase), Al_2Cu (θ phase) and Al_7Cu_2Fe on the size of a few micrometers, and (iii) grain boundary precipitates similar to $Mg(Zn,Cu,Al)_2$ of about 50-100 nm in size [4]

Cu distribution has a significant impact on the alloy's susceptibility to localized corrosion: Pitting corrosion is usually linked with the galvanic interaction of Cu or Fe-containing IMPs and the Al matrix beside them [5]. IGC is often associated with the micro-galvanic reaction between the more noble Cu-containing grain boundary precipitates and the less noble PFZs along the grain boundaries [4]. Corrosion can lead to the dealloying of Cu-containing IMPs and matrix leading to accelerated corrosion of the matrix adjacent to the Cu precipitates [6]. Extensive corrosion research has been conducted on the wrought from of these alloys, and much of the localized corrosion susceptibility is attributed to the chemistry and distribution of these Cu-containing precipitates. The localized corrosion susceptibility of the cast counter-parts of these alloys has received significantly less attention [7]. This research is focused on understanding the effect of the CDS casting processing route on the localized corrosion susceptibility of the granular microstructure of AA7050 (Al-xZn-xMg-xCu) in the peak-aged T6 condition relative to the benchmark wrought processed counterpart. It is believed that since the CDS casting processing route results in a granular structure, it will have similar susceptibility to localized corrosion as seen in the wrought counterpart. The following project aims to prove or disprove this hypothesis.

This thesis contains seven chapters: Chapter 2 provides a critical review of the relevant literature about the corrosion of AA7xxx alloys. Chapter 3 specifies the research objectives by which the hypothesis will be judged. Following this, Chapter 4 documents the experimental methods employed to satisfy the research objectives. The experimental results are presented in Chapter 5 and discussed in Chapter 6. Chapter 7 will conclude the project.

Chapter 2: **Literature Review**

2.1 *High Strength Aluminum Alloys*

An Al alloy’s properties are dependent on the alloy composition and microstructure as determined by the chemistry, processing conditions and heat treatments. Only a few number elements have sufficient levels of solubility to be used as major alloying elements: Mg, Zn, Cu and Si can be used, while other elements with less than 1% solubility in Al such as Mn, Cr, Zr, and Ti can be used in small amounts as grain refiners. Alloying is very important part of designing high strength Al alloys due to the inherently low strength of pure Al (only ~10 MPa). The most common and simplest technique for improving strength is solution hardening. Solution hardening is where alloying elements are added which have large amounts of solid solubility over a wide range of temperatures and can remain in solution after many heat treatments [8].

The most effective technique in improving an Al alloy’s strength is precipitation hardening which can result in alloys with strengths up to 800 MPa. Precipitation hardening works by using an alloying element that has a solubility that decreases with temperature. Precipitation hardening is broken down into three stages:

1. Solutionizing at a temperature in a single phase region which dissolves all the alloying elements to reach a state of homogenization
2. Quenching to room temperature to reach a state of supersaturated solid solution
3. Aging by heating at a moderately elevated temperature to nucleate and grow small finely dispersed precipitates.

Though precipitation hardening is well studied, the mechanisms behind this process are still not well understood. The general understanding is that Guinier-Preston (GP) zones and several intermediate phases form first before transforming into the equilibrium precipitate phase. GP zones are defined as the small clustering of alloying elements along preferred crystal directions in the Al lattice. Manipulations to this process can greatly enhance the results by precise thermo-mechanical processing such as duplex aging, retrogression and re-aging [8]. Hardness can be maximized by cold working between the quenching and aging steps. This process maximizes the dislocation density and provides more sites for heterogeneous nucleation. Grain refinement has a moderate influence on strength but has a strong influence on fracture toughness. Al alloys can be refined by small additions of low solubility elements such as Ti and Zr which provide grain nucleation sites. Dispersoids are formed from elements (Cu, Cr, Zr, and

Mn). The function to inhibit recrystallization by forming insoluble particles that can pin grains.

High strength Al alloys generally contain as many as 10 alloying elements. This alloying results in a complex microstructure containing many equilibrium and non-equilibrium phases. Non-equilibrium phases are essential to achieving the highest strength and are achieved by careful thermal processing. A diverse microstructure with many different elements and chemistries results in a complex corrosion behavior with many different mechanisms. Of particular concern is the influence of impurity elements which are quite often found in the alloy due to the many number of alloy additions and processing operations. Impurities (most commonly Fe) can form insoluble compounds called constituent intermetallics particles (IMPs). These IMPs can be found in large size and irregular shape ranging from 1 to 50 μm. These IMPs form during solidification and are difficult to dissolve/disperse even with the use of thermo-mechanical processing. Often these IMPs can be found clustered together with different chemistries, which enhance their electrochemical behavior relative to the surrounding matrix [8].

2.2 *Processing of AA7050*

As discussed in the previous section, the processing route of an aluminum based material will have a significant influence on its microstructure and properties. The following section goes over the main processing routes of AA7050: solidification (casting), mechanical processing (rolling) and thermal processing (heat treatments).

2.2.1 *Issues with casting*

Typically casting of AA7050 and similar alloys properties do not reach full potential due to microstructural deficiencies. Casting AA7050 comes with many challenges due to coarse intermetallic phases, large grains, significant elemental micro-segregation, solid solubility limitations and most importantly large amounts of macro-segregation [2]. This large amount of macro-segregation often leads to high amounts of porosity, built up residual stress and ultimately hot tearing (cracking).

These casting issues are understood by the solidification mechanics of AA7xxx range. AA7xxx are Al-Zn based alloy and have a typical phase diagram as shown below in Figure 2-1. This Al-Zn phase diagram has been well studied for over 80 years [9]. Issues during solidification arise due to the low partition coefficient "k" which is the ratio between the slopes of the liquids line (the boundary between L and L + α $Al_{(s)}$) and the solidus line (the boundary between L + α $Al_{(s)}$ and α $Al_{(s)}$). Typical AA7xxx chemistries cross this boundary of the phase diagram. Because of the low partition coefficient, there is significantly high amounts of solute rejection at the solidification front as described by the Scheil model below in Figure 2-2a. This rejection leads to a drastic difference in chemistry between the solidification front and surrounding liquid [10]. This difference continues to increase, prolonging the freezing time of the remaining liquid phase. More importantly, the solute pile up leads to a large concentration gradient (G_L) that when higher than the thermal gradient, promotes perturbation of dendritic formation and extends primary dendritic growth. This dendritic growth results in more liquid entrapment and thus, more shrinkage during the final stages of solidification relative to the surrounding α Al phase. This entrapment results in the formation of shrinkage pores which must be avoided to prevent hot tearing from occurring [2], [11].

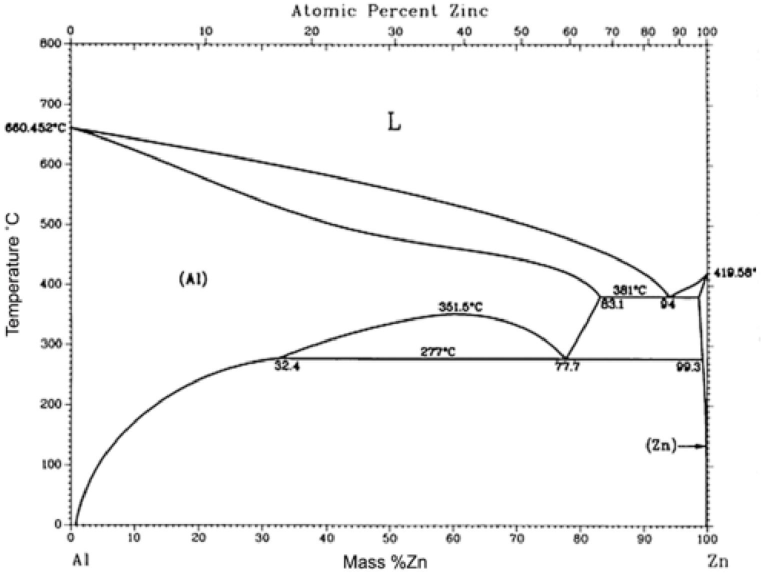

Figure 2-1: Generic Al-Zn phase diagram [9].

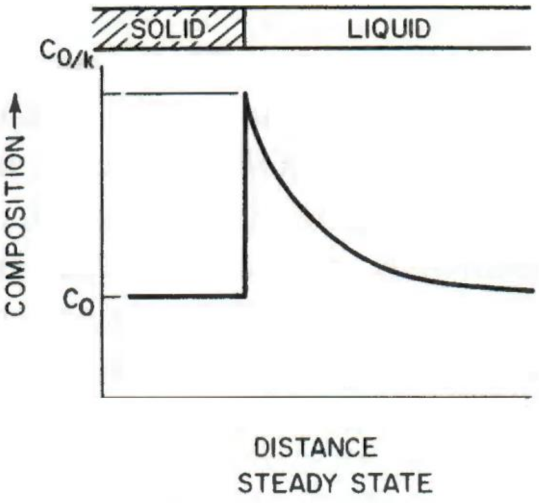

$$\frac{G_L}{R} \geq -\frac{m_L C_S^*(1-k)}{kD_L}$$

Figure 2-2: (a) Solute redistribution during solidification with limited liquid diffusion and no convection [10]. (b) General constitutional supercooling criterion.

Currently, AA7050 is mainly produced by three types of casting: sand casting, permanent mold cast and die casting. Large production is restricted to direct chill (DC) semi-continuous casting into large ingots or slabs. This process uses water-cooled molds which can discourage dendritic growth by controlling the solidification rate (R). Billets then undergo thermo-mechanical processing to (i) reduce the size, number, and density distribution of shrinkage pores, (ii) reduce grain size and (iii) produce sub-structure to increase mechanical properties by use of plastic deformation [11].

2.2.2 *Controlled Diffusion Solidification (CDS) Casting*

CDS is a new casting technique that has been developed to cope with the issues of hot tearing in AA7xxx alloys and, thus enable the application of near net shaped castings. CDS works by manipulating the solidification mechanics to avoid extreme amounts of macro-segregation and extensive primary dendritic growth. The CDS process involves mixing two precursor-melts at specific temperatures and compositions: As seen below in Figure 2-3a, Alloy 1 is essentially pure Al, while Alloy 2 is near the eutectic chemistry. The two melts are balanced in a ratio such that when the two are mix macroscopically together, the bulk concentration equals that of the desired alloy chemistry range. The two melts are heated 15 °C above their respective liquidus temperatures and mixed macroscopically just before casting. Due to the discrepancy in melting temperature between alloy 1 and 2, initial mixing results in copious nucleation of alloy 1 in the melt before solidification as seen below in Figure 2-3b.

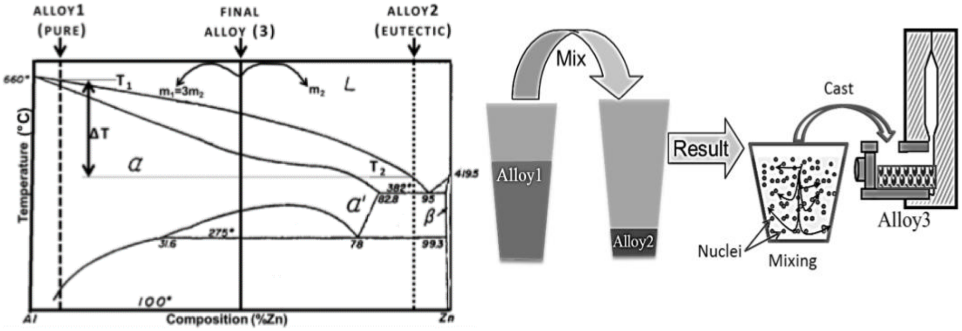

Figure 2-3: (a) CDS melt chemistry, (b) CDS casting process [2].

This process avoids the problem of hot tearing by manipulating the concentration profile ahead of the solidification front: as seen below in Figure 2-4a. Since alloy 2 has a lower melting temperature than the nucleated alloy 1, it thus becomes the bulk liquid concentration. Therefore the CDS process avoids the solute buildup ahead of the solidification front. This buildup greatly reduces the amount of solute segregation and dendritic growth resulting due to lowering the driving force for supercooling. This effect is illustrated below in Figure 2-4b and c showing the differences in the resulting microstructure: The conventional casting route results in large α Al dendrites and significant macro-segregation, while the CDS casting route results in a consistently equiaxed granular microstructure.

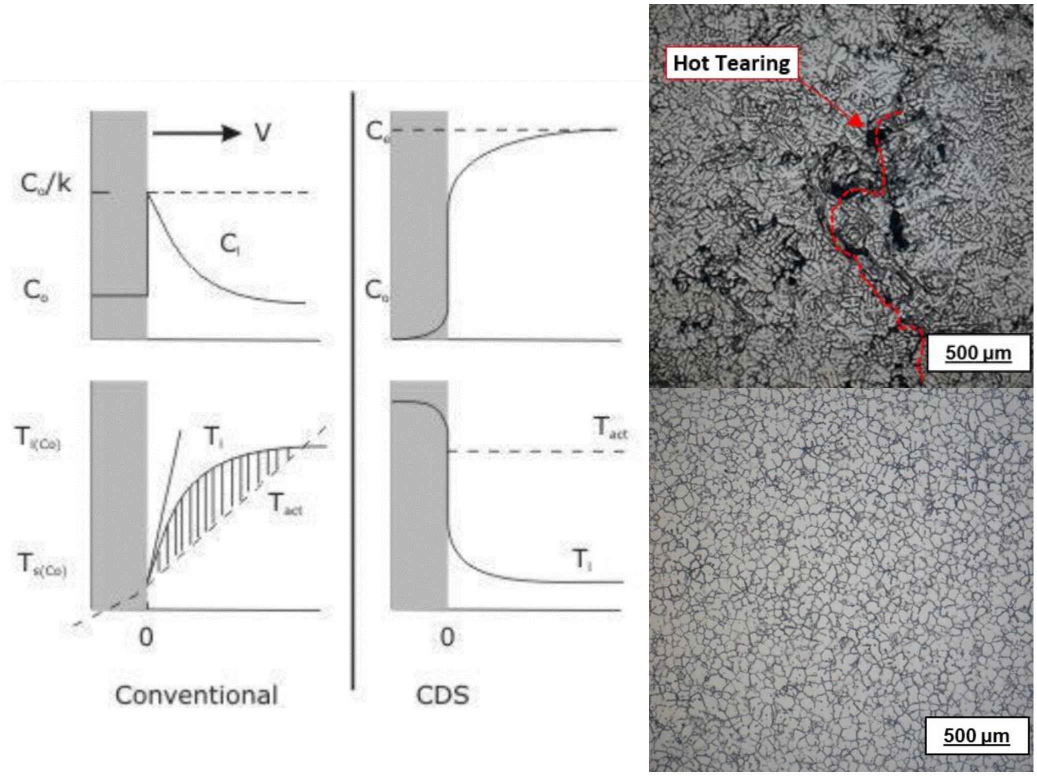

Figure 2-4: (a) Plane front solidification: Conventional vs. CDS cast (b) Conventional cast microstructure (c) CDS cast microstructure.

2.2.3 *Wrought Processing*

Wrought materials are produced by rolling large slabs or billets as thick as 5000 mm down to 15 to 35 mm. Production involves DC casting followed by homogenization, hot rolling, cold rolling and then aging [11]. This process requires large inputs of energy in the forms of heating up to 500°C and mechanical deformation [8]. The success of the wrought processing route is measured the reduction in the porosity (formed during the DC casting) achieved. Thermo-mechanical processes must be optimized to reach the full mechanical strength of the alloy. Higher amounts of rolling reduction result in greater reduction of porosity.

2.2.4 *Heat Treatments*

Since AA7xxx alloys have the ability to be precipitation hardened, there are many different types of heat treatments, primary and secondary to improve different mechanical properties and decrease corrosion susceptibility. Since AA7xxx alloys derive their strength from the precipitation hardening and manipulation of the η phase ($MgZn_2$), there are many complex thermo-mechanical processes used for its optimization. Common heat treatments of AA7050 are listed below in Table 2-1.

Table 2-1: Common AA7050 heat treatments.

Heat Treatment Designation	Characteristics
O	Annealed
T4	Solution heat-treated and naturally-aged (at room temperature)
T6	Solution heat-treated and artificially aged for peak strength
T7451	Multi-stage solution heat treating and artificially aging to decrease corrosion susceptibility
T7651	Multi-stage solution heat-treating and artificial aging to decrease corrosion susceptibility with higher strength

2.2.5 *Microstructure Features*

The bulk of the microstructure of AA7050-T6 is comprised of the α Al phase. This phase has an FCC crystal structure and solubility for Mg, Zn, Cu. AA7050-T6 is precipitation hardened by the heat treatment applied (T6), which results in finely dispersed strengthening η' (semi-coherent) and η (incoherent) phase ($MgZn_2$) precipitates on the nm scale. Major alloying elements are segregated to precipitates mostly found on the grain boundaries. Grain boundaries are distinctly recognized by a PFZ containing >96% Al with small amounts of Zn and Mg. Between PFZs in the middle of the grain boundary, are grain boundary precipitates. The most common grain boundary precipitate is a semi-coherent η' precipitate, which is several times larger than the dispersed η hardening precipitate. This grain boundary structure is illustrated below in Figure 2-5 for an Al-Mg-Zn alloy. Additions of Cu manipulate the nucleation of η' precipitate increasing density (ppt/m^3) and hardness (as shown below in Figure 2-6), but, as a result, several types of grain boundary precipitates form. Excess amounts of Cu segregate to the η' grain boundary precipitate to form $Mg(Zn,Cu,Al)_2$. The majority of the remaining Cu is segregated to IMPs θ-phase (Al_2Cu) and the S-phase (Al_2CuMg) at the grain boundaries. Heat treatments cause some of these Cu-based IMPs to dissolve, but Fe-containing IMPs transform into Al_7Cu_2Fe [8]. S, θ, and Fe-based IMPs vary considerably in stoichiometry with solubility for Zn, Mn and Si and the science is not well understood. There is considerable evidence supporting the notion of IMP clustering: It has been observed in many studies of AA2xxx and AA7xxx alloys that the S, θ, and Fe-based IMPs cluster together. This is a concerning microstructure heterogeneity as this clustering can promote the formation of stable corrosion pits [8].

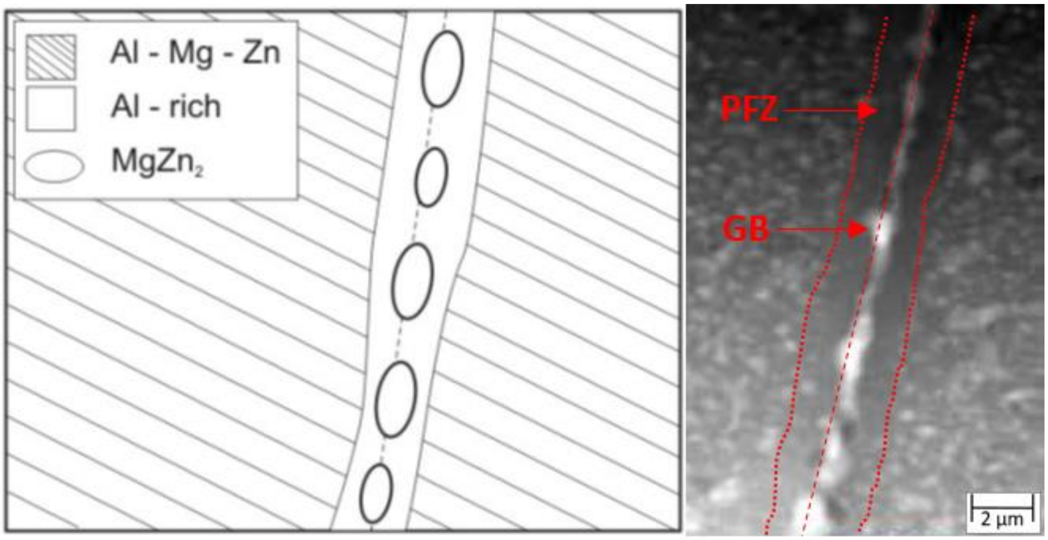

Figure 2-5: (a) Schematic of hypothetical grain boundary in an Al-Zn-Mg alloy. This schematic indicates the different chemistry that exists in the grain interior (b) Bright field TEM image of high angle grain boundary in AA7075-T651, revealing grain boundary precipitates ($MgZn_2$) and a distinguishable PFZ [8].

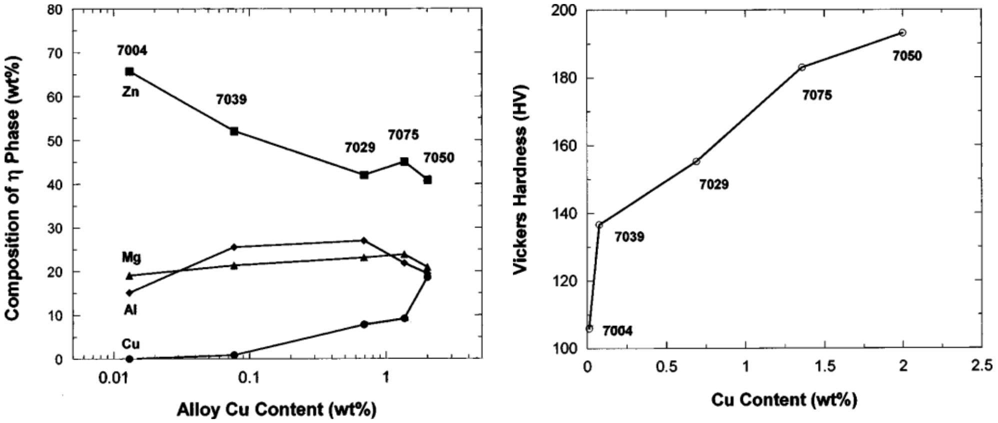

Figure 2-6: (a) Composition of η phase precipitates on grain boundary as a function of alloy Cu content in AA7xxx-T6. (b) Microhardness vs. Cu content curve showing that Cu addition increases the hardness of AA7xxx-T6. [12]

2.3 *Corrosion of AA7xxx Alloys*

AA7xxx alloys are typically susceptible to some form of localized corrosion. Wrought alloys are typically most susceptible to IGC. Typically, these alloys suffer from localized corrosion due to the large separation of the anodic and cathodic reactions. The basic anodic reaction is metal dissolution ($Al \rightarrow Al^{3+} + 3e^-$) and the cathodic reactions are oxygen reduction ($O_2 + 2H_2O + 4e^- \rightarrow 4OH^-$) and hydrogen evolution ($2H^+ + 2e^- \rightarrow H_2$) in acidified environments (solution or corrosion pits) where aluminum ion (Al^{3+}) hydrolysis takes place: ($Al^{3+} + 6H_2O \rightarrow Al(H_2O)_6^{3}$). The interaction between the cathodic and anodic reactions and the matrix determine the types of localized corrosion observed. Classic examples of localized corrosion include IMP etch-out, pitting corrosion, IGC, trenching and exfoliation corrosion.

Pure Al has low corrosion susceptibility due to its formation of a stable protective oxide film that has a strong affinity to the surface (passive layer). In most environments, the passive layer also can reform quickly if it is damaged (re-passivation). In aerated solutions, this layer is especially stable but is susceptible to pitting in solutions containing halide ions (such as Cl^-) because of the formation of a very soluble chlorinated aluminum oxide ($Al^{3+}[nCl^-]OH_2^+$) that prevents the formation of the passive layer [8] [13].

High strength Al alloys such as AA7050 are heterogeneous materials, therefore in corrosive environments, there is a mix of Al-Mg oxides (alloys with Mg) and Al oxides on the surface. Al oxidizes from exposed IMPs on the surface as well as it does from the exposed matrix. Since most surfaces are mechanically finished, there is near-surface damage layer present and shingling occurs during the finishing process, where the matrix is spread across the surface and cover the IMPs since IMPs are harder to deform than the matrix. Matrix and IMPs form different oxide structures that are not continuous, resulting in a significant defect site where pitting corrosion can initiate [8].

2.3.1 *Pitting Corrosion*

“Pitting corrosion is localized accelerated dissolution of metal that occurs as a result of a breakdown of the otherwise protective passive film on the metal surface” [14]. Pits usually form in aggressive environments where halogens, particularly the ubiquitous Cl^- ion, are present. In Al alloys, there are two main types of pits: metastable and stable pits: metastable pits can form well below the characteristic pitting potentials associated with stable pits. They last only a few seconds and may grow to a few micrometers ins size before re-passivation takes place. Stable pitting occurs when the pit can produce an local environment that allows for autocatalytic reactions to take place. Pit environments become more aggressive with a decrease in local pH and increase in local halogen concentration. Pit shapes can either be isotropic or microstructural oriented (anisotropic) [14].

Pit initiation is a complex process. There are three proposed models: adsorption mechanism, penetration mechanism, and film breaking mechanism. Adsorption model focuses on the effect of the adsorption of aggressive anions Cl^-. The penetration model focuses on the effect of anion penetration and ion migration through the passive film. Film breaking focuses on the effects of defects in the film as the source of pit initiation.

Above the E_{pit} stable pits can form and can continue to grow through autocatalytic reactions, preventing re-passivation. Pit growth is controlled by three factors: charge-transfer, ohmic control, and mass transport. The weight of these factors is influenced by the alloy, environment, and the shape of the pit itself. Studies by Frankel et al. [14] found that pit growth is initially controlled by ohmic control, but more developed pits are restricted by mass transport.

2.3.2 *Effects of Microstructure on Corrosion*

With respect to corrosion, the two most important microstructural features are grain structure and distribution of second phases including constituent IMPs, dispersoids and strengthening precipitates. On the macro-scale, clustering of constituent IMPs play a prominent role in pitting susceptibility. Dispersoids and strengthening precipitates differ from the surrounding matrix in electrochemical reactivity, which can lead to micro-galvanic corrosion. The effect of these features is discussed in the following sections.

2.3.3 *Corrosion around IMPs*

IMPs are either anodic or cathodic relative to the matrix surrounding them. Corrosion at these sites usually result in two different types of pit morphologies: Circumferential pits appear as trenches around intact IMPs particles, which serve as an active cathode. The associated anodic dissolution is restricted to the surrounding matrix. This type of pitting is not as concerning if the current density × pit depth ($i \cdot r$) is below 10^{-2} A/cm, which is the critical value determined for the pit to be able to grow rapidly enough to establish a sufficient diffusion path for an oxygen gradient. It has been shown that this $i \cdot r$ value is typically too low for this trenching to develop into stable pits [15]. The other type of pitting occurs due to selective dissolution of the IMPs, which serve as active anodes. This dissolution often results in deep pits that have remnants of the particle in them. In AA7xxx alloys, an example of this is the dealloying of the S phase. A model of S-phase dealloying is shown below in Figure 2-7: under neutral pH conditions: Mg and Al anodically dissolves preferentially from the Al_2CuMg phase leaving a Cu-enriched particle with high surface area. Dissolution of Cu clusters leads to redisposition on the surface creating cathodic sites which enhance the kinetics of oxygen reduction due to the increased nobility of the solution relative to the matrix. This redistribution of Cu causes secondary pitting to occur increasing corrosion susceptibility. It has been shown that the morphology of the redistributed Cu has a large impact on Cu enhancement of the cathodic reactions: Rapid dissolution rates lead to more porous network structures allowing for more noble metal to be released into the solution while slow dissolution rates allow for diffusion to maintain a stable surface structure [8], [16]. It has been suggested that a Cu concentration over 25 at% in the Al_2CuMg phase leads to dealloying and dissolution rates high enough to support the formation of a porous Cu-rich network, which further releases clusters of oxidized and unoxidized Cu into the solution [8], [16], [17].

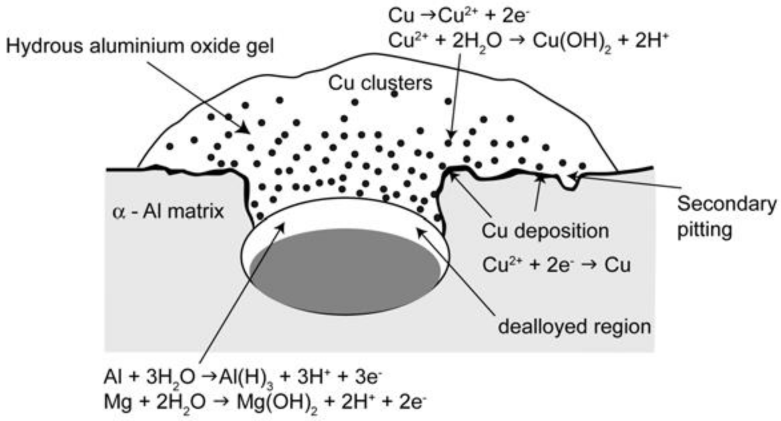

Figure 2-7: Schematic of S-phase (Al_2CuMg) dealloying contained in an Al matrix. Anodic polarization results in preferential loss of the Al and Mg. This leads to a Cu-rich network, which when dissolved can enhance cathodic sites causing secondary pitting [8] [16].

2.3.4 *Particle Clustering and Corrosion*

Awareness of the effects of IMP clustering has increased with recent research. Severe pitting corrosion has long been attributed to IMP clustering, but only recently has a better understanding of the relationship has been garnered. Hughes et al. [8] studied the electrochemical boundary between the conditions for metastable and stable pits in AA2024-T3 and AA7075-T6 by measuring the current transients on corroding surfaces and calculating the associated $i \cdot r$ value in a 0.1M NaCl solution. The current transients revealed three major events:

1. Spontaneous nucleation/passivation events over a short period.
2. Metastable pitting events with life a span up to several seconds, followed by decay to background currents.

3. Stable pitting events with increasing transient current peaks and regressions to a constant value, which is an indication of ongoing growth.

As seen next in Figure 2-8, it was determined that a higher density of IMPs result in a higher level of electrochemical activity. This electrochemical activity was explained by excessive trenching around the IMP cluster leading to the quicker development of stable pitting. It was also reported by Hughes et al [8] that the initiation of new corrosion sites occurred within rings of corrosion product on AA2024-T3. These rings formed in the early stages of immersion and the sites inside were characteristic of high amounts of H_2 evolution and extensive grain boundary attack, which occurred before or during the trenching around IMP clusters. Below the surface of these corrosion ring sites was almost exclusively IGC penetrating at most 60 μm within 120 mins of exposure to 0.1 NaCl solution. This IGC preceded the development of any stable pitting suggesting that IGC proceeds before any substantial grain etchout [8], [18]. T chronology of attack leading to stable pitting shown in Figure 2-9 was proposed This model suggests that trenching is either a secondary corrosion process or that there are other factors that can initiate stable pitting at IMP clusters. However, work done by Zhou et al. [19] [20] showed that stable pits could be established by penetration through large S/θ composite IMP: an indication that many different avenues exist to induce stable pitting.

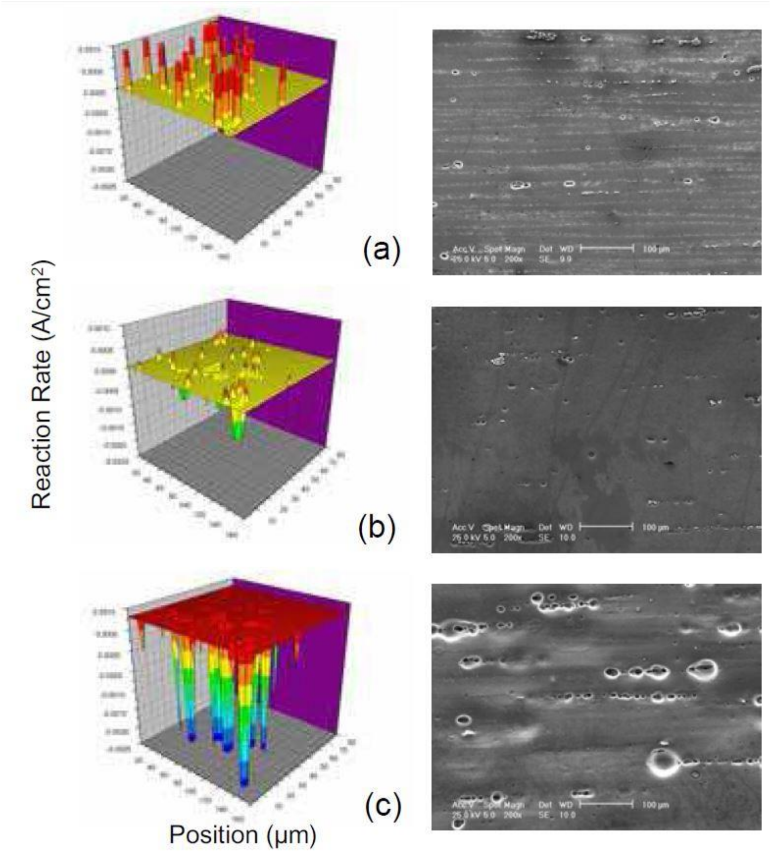

Figure 2-8: 3-D representations of the spatial variation in electrochemical reaction rate in AA7075 at a potential -0.8 V_{SCE} in aerated 0.1 M NaCl and SEM images of AA7075 after 24 h exposure under free corrosion conditions in aerated 0.1 M NaCl solution (a) pH 2.5, (b) pH 6 (c) pH 12 [8].

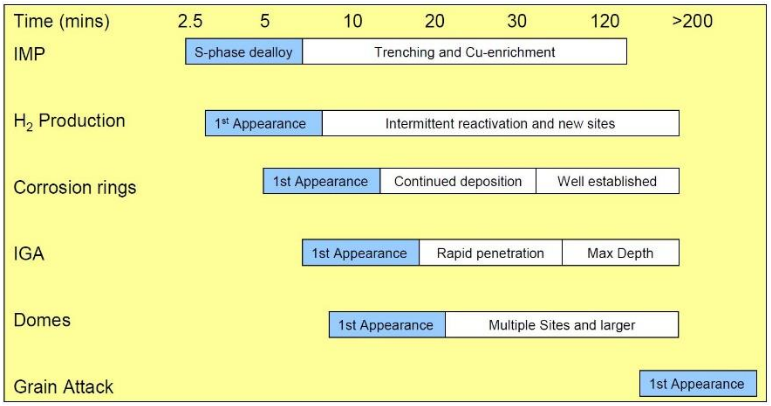

Figure 2-9: Chronology of attack in AA2024-T3 proposed by Hughes et al. [8] [18].

2.3.5 *Intergranular Corrosion (IGC)*

The proposed mechanisms of IGC has always been under a lot of scrutiny and debate. Currently, it is understood that it is a process by which the grain boundary region is preferentially attacked because of its anodic nature relative to the bulk beside it. IGC can initiate from the following locations: (i)IMPs located on the surface, (ii) base of corrosion pits, and (iii) grain boundaries exposed on the surface. IGC penetrates faster than pitting and has been shown to have a more detrimental effect on corrosion fatigue resistance [8].

In Al-Cu alloys Al_2Cu precipitates cause the adjacent grain boundaries to become more anodic and, therefore become prone to more attack. In Al-Mg alloys, the Mg_2Al_3 precipitate is less noble than the grain boundary and, therefore is preferentially attacked. Extensive grain boundary attack can be avoided through careful processing as the distribution of the second phase particles has a significant impact on the alloy's susceptibility to IGC due to their differences in composition and electrochemical activity relative to the grain boundaries. The PFZ also plays a large role in IGC susceptibility because it is depleted in particular alloying elements resulting in large compositional difference relative to the bulk matrix. In high strength Al alloys IGC usually attributed to anodic dissolution of:

i. PFZs where the alloying elements are depleted.
ii. Large strengthening precipitates on the grain boundary
iii. Grain boundaries that have segregated impurity elements.

In Al-Cu-Mg alloys many studies suggest that Al_2Cu precipitates form at grain boundaries with a Cu-depleted PFZ that is anodic relative to the Al_2Cu precipitate and the matrix. IGC is then attributed to micro-galvanic corrosion occurring adjacent to Cu- depleted areas. IGC is promoted even more when the S-phase (Al_2CuMg) is preferentially formed on the grain boundary, which enhances the anodic dissolution of the PFZ [8]. Not all IGC can be explained by micro-galvanic corrosion with second phase particles: studies [21] have shown that high levels of stored energy due to high grain boundary misorientation also lead to preferential grain boundary attack.

In AA7xxx the most common grain boundary precipitate is the η/η' phase ($MgZn_2$), which is relatively active relative to the matrix. With IGC, micro-galvanic coupling occurs between the η phase and the matrix adjacent to the precipitate [22]. However, the IGC susceptibility of AA7xxx alloys is highly influenced by the heat treatment and degree of segregation to the grain boundaries. The T7 heat treatment (over-aging) provides the lowest IGC susceptibility by reducing the differences in chemistry across the grain boundaries.

Exfoliation is also a concern in AA7xxx alloys and is closely tied to IGC. Especially in cold-worked materials where grains are elongated and flattened out by the deformation, IGC attack of the transverse planes can run along the alloy surface. Exfoliation is characterized by corrosion lifting off layers of grains because of corrosion product swelling in the grain boundaries below that layer [8].

2.4 *Electrochemistry and Corrosion of AA7xxx*

There have been many electrochemical tests conducted on Al-alloys to quantify the characteristics of corrosion susceptibility and identify the main modes of corrosion. With the use of polarization testing, two characteristic potentials can be determined: breakdown potential E_b (or pitting potential E_p for pitting corrosion specifically) and the re-passivation potential E_R at which localized corrosion stops. These potentials are influenced by the alloy chemistry and the environment that it is exposed in. Alloys with higher E_b and E_R generally suggest lower susceptibility to pitting and IGC corrosion, but there are many other factors involved such as microstructural heterogeneities that keep this from being an irrefutable method of comparison.

2.4.1 *Effect of Alloying Elements on E_{corr}*

In AA7xxx alloys the corrosion potential (E_{corr}) is determined by the composition of the bulk Al matrix that makes up most of the volume of the material. E_{corr} is not greatly influenced by second phase particles on the small scale. The effects of the major alloying elements are shown below in Figure 2-10: each alloying element has a significant impact on E_{corr} within its respective solubility limit in Al. Supersaturation resulting in secondary phase precipitation has little impact on E_{corr}. Rather E_{corr} is influenced by the concentration of elements in the solid solution. Thus, heat treatments make a big difference on E_{corr} by controlling the amount of elements in the solid solution [23]. These measurements can be useful to understand the effectiveness of heat treatments and measuring the amount of Cu or Zn left in the solid solution to gauge the success of solution heat treatments.

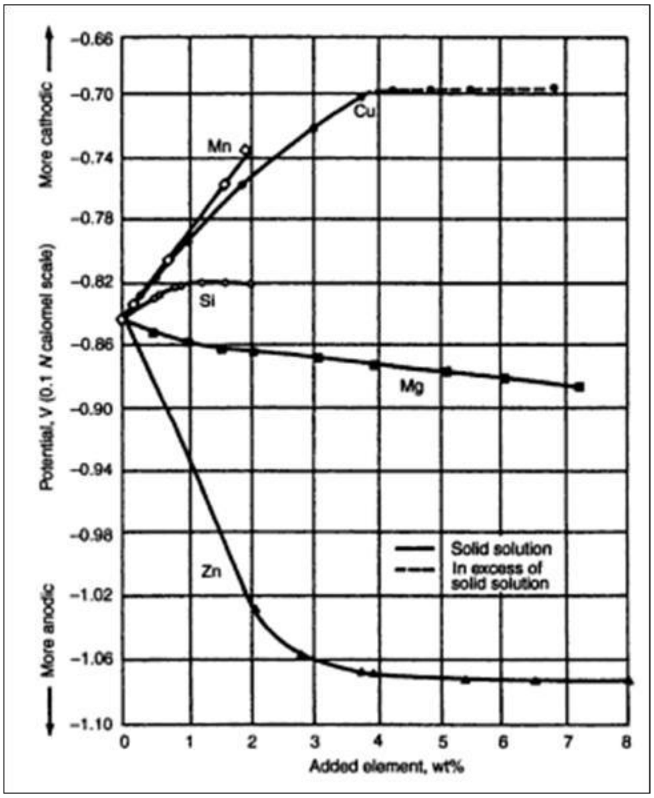

Figure 2-10: Effect of major alloying elements on electrolytic solution potential E_{corr} of Al. Potentials are for high-purity binary Al alloys solution heat-treated and quenched. The data are obtained using a solution of 53 g/l NaCl plus 3 g/l H_2O_2 maintained at 25 °C. [23]

2.4.1 *Effect of Cu on E_b*

Studies were conducted by Meng et al., to understand the effect of Cu content on the corrosion behavior of the AA7xxx series range. Five alloys were compared that spanned the range of Cu in AA7xxx from Cu free to 2 wt%. Effect of corrosion was quantified by measuring the breakdown potential: results of testing are shown below in Figure 2-11: alloys containing Cu had two breakdown potentials which increased logarithmically with Cu wt% [12]. A summary of the breakdown potentials calculated is shown below in Table 2-2.

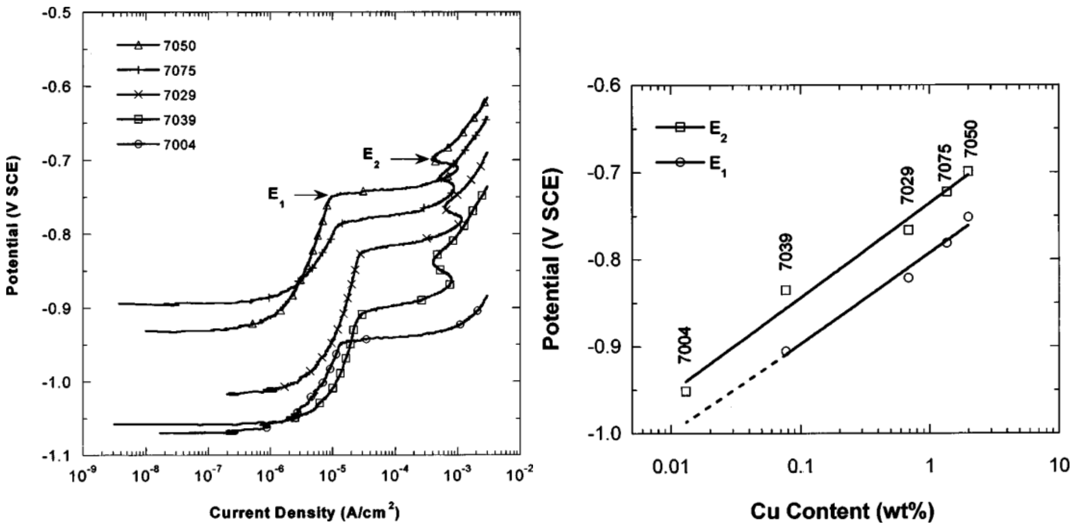

Figure 2-11: (a) Potentiodynamic polarization curves for AA7xxx-T6 alloys in deaerated 0.5 M NaCl at pH 3.56 with a scan rate of 0.2 mV/s. (b) Correlation between the breakdown potentials in deaerated 0.5 M NaCl at pH 3.56 and the alloy Cu content [12].

Table 2-2: Breakdown potentials for AA7xxx-T6 in deaerated 0.5 M NaCl at pH 3.56 [12].

Alloy	E$_1$ (mV$_{SCE}$)	E$_2$ (mV$_{SCE)}$	E$_1$- E$_2$ mV
7004	N/A	-951 ± 3	N/A
7039	-905 ± 3	-835 ± 3	70
7029	-821 ± 3	-766 ± 3	55
7075	-780 ± 3	-720 ± 2	60
7050	-751 ± 3	-699 ± 1	52

Further work was conducted by Zhao et al. [20], [19] reported that the second breakdown reported by Meng and Frankel [12] was an artifact caused by the formation of a near surface layer during polishing. The layer contained a microstructure vastly different than the bulk with a grain size of ~10 nm and the absence of strengthening precipitates. Instead, the polishing resulted in the formation of Zn-rich bands, which causes the preferential dissolution observed. An etching method was proposed to remove the damaged layer before conducting polarization measurements.

.

Chapter 3: Research Objectives

Based on the literature, it is expected that CDS processing of AA7050 will produce a completely equiaxed microstructure. This casting process is expected to render the CDS material susceptible to certain types of localized attack: specifically pitting and/or IGC, similar to the wrought counterpart. It is important to understand the extent of the relative difference in the overall corrosion susceptibility of AA7050 and determine if the CDS processing route provides an acceptable level of corrosion susceptibility relative to the wrought processing route, which is considered as the benchmark in this study.

This research aims to determine the acceptability and identify the key differences in the corrosion susceptibility of the CDS material vs. the wrought material. This identification was accomplished by characterizing both the microstructure and localized corrosion susceptibility and then linking the different aspects of the CDS microstructure against the wrought microstructure to the relative difference in corrosion susceptibility observed. The overall impact the CDS processing route on the localized corrosion was then confirmed by a longer term cyclic acidified salt fog exposure. The following sections layout the specific research objectives of each major task.

3.1 *Microstructure Characterization*

The specific objective here was to characterize the localized corrosion susceptibility of the AA7050 CDS material. The microstructure was fully characterized and compared against its wrought counterpart. This was done to understand the effect of the CDS processing route on the chemistry, size and distribution of the second phase particles and grain boundary segregation as both have a direct impact on the corrosion mode and its penetration.

This was accomplished by comparing the grain size distribution and aspect ratio and degree of grain boundary misorientation. Strengthening precipitates and grain boundaries were characterized by APT and Auger electron spectroscopy to compare the concentration of Cu in the grain boundary precipitates and the width of the PFZ. Both can have a significant impact on the corrosion activity at the grain boundary and the extent of dealloying around S phase intermetallics during corrosion.

3.2 *Localized Corrosion Characterization*

The specific objective here was to characterize the localized corrosion susceptibility through electrochemical testing: Potentio-dynamic tests were used to determine E_{corr} and E_b. Potentiostatic tests were conducted just above E_b to observe the dominant corrosion mode and the relative corrosion susceptibility. Cross-sectioning was conducted on the resulting corroded samples to compare corrosion modes both during initiation (short-term testing) and propagation (long-term testing). Also, the depth of corrosion was measured to compare the corrosion susceptibility of each material. OCPs of fracture surfaces with increased grain boundary area were measured to compare the reactivity of the grain boundaries. Differences in overall corrosion susceptibility found during electrochemical testing was validated by the use of ASTM G85-A2: acetified cyclic salt spray testing under more realistic conditions. Cross-sectioning was conducted to compare the corrosion mode and extent. Complementary weight loss measurements were also conducted to quantify the corrosion extent.

3.3 *Linking Corrosion Susceptibility to Microstructure*

The specific objective here was to link relative differences in the electrochemical behavior with relative differences in the microstructure. This is done by interrogating the main culprits that are believed to have the greatest influence on the localized corrosion mode. These influences include: (i) type of coarse IMPs such as Al_2CuMg (S), Al_2Cu (θ) and Al_7Cu_2Fe, (ii) composition of grain boundary precipitates and PFZ (iii) overall distribution of the Cu content across the grain boundary region.

Chapter 4: **Experimental Methods**

4.1 *Materials*

CDS-processed samples were cast by the Light Metals Casting Research Centre (McMaster University) via the CDS processing route. Alloy 1 (Al-2.8Mg-0Cu) and Alloy 2 (Al-23.8Zn-8.68Cu) were each heated 10°C above their liquidus temperatures, mixed and cast into a tilt pour gravity fed mold to make tensile bars, as shown in Figure 4-1. The two alloy melts were mixed in a ratio such that a third alloy, Alloy 3 (Al-6Zn-2.2Mg-2.3Cu), was achieved.

Figure 4-1: CDS tilt pour gravity fed as-casted tensile bar mold.

Counterpart wrought-processed samples were prepared from commercial sheet purchased from Metals Samples Company (Munford, AL), which was provided in the T7651 condition. Table 4-1 compares the bulk composition of the two materials, as determined by using Glow Discharge Optical Electron Spectroscopy (GDOES). There is some divergence between the composition of the CDS and wrought materials:

The CDS material has 0.3% less Cu, 1% less Zn and 0.4% less Mg. All the elements in the wrought and CDS material were within AMS 4201 standard range for specified for AA7050 [24] with the exception slightly low Zn for the CDS. For the CDS alloy, extra Ti was added as a grain refiner to prevent excessive grain growth during solidification by promoting more even distribution of the eutectic phase [25]. The CDS having lower 1% less Zn, may result in having a more noble breakdown potential [23]. Though overall, the chemistry is similar such that any major differences in the localized corrosion resistance will likely be due to differences in the microstructure heterogeneities and the nature of the Cu distribution intrinsic to the processing route rather than the bulk chemistry.

Test samples from materials were heat treated to the T6 condition. This heat treatment involved a solutionizing heat treatment at 475 °C for 2 h followed by a quench in water and then a one-step aging treatment at 120 °C for 24 h followed by cooling in air. All heating was controlled at ramp speed of 100 °C/h to avoid incipient melting.

Table 4-1: Bulk composition of starting materials as determined by GDOES

Element (Wt%)	**7050 Wrought**	**CDS 7050**		**AMS Standard 4201** [24]
Source	**Mill Cert**	**Expected**	**GDOES**	
Cr	0.01		<6 ppm	Max 0.04
Cu	2.32	2.3	2.03	2-2.6
Fe	0.08		0.07	Max-0.15
Mg	2.38	2.2	1.98	1.9-2.6
Mn	<0.01		0.02	Max-0.1
Ni	Not Detected		<33 ppm	Max 0.5
Si	0.07		0.01	Max-0.12
Ti	0.06	0.06	0.38	Max 0.06
Zn	6.62	6	5.62	5.7-6.7
Sn			Not Detected	Max 0.5
Al	88.46	89.44	89.67	88.62-90.4

4.2 *Microstructure Characterization*

4.2.1 *Light Optical Microscopy*

Orthogonal planar sections were cut from each material for microstructural examination using a Keyence VHX digital microscope, model VHX 5000 light optical microscope. Samples were cold mounted in epoxy, ground to 4000 grit and then polished to 1 µm using diamond pastes and standard metallographic procedures. The final step of polishing was conducted using a water-free silica colloidal suspension

(OPS). Samples were etched with Keller's etchant (190 mL distilled water, 5 mL of HNO_3, 3 mL of HCl , and 2 mL HF). The etchant was applied for 8-14 s and then rinsed with water. Each unique plane was defined by the associated normal direction to each: Longitudinal (rolling) (L), Transverse (T) and Short Transverse (S). The CDS material was sectioned perpendicular to the two orthogonal normal directions: Cross section (CS) and Longitudinal (L). The CDS cross-section plane is parallel to the longitudinal (pouring) direction and is indifferent about tensile bars vertical axis. Figure 4-2 shows an orthogonal view of the microstructure of each material.

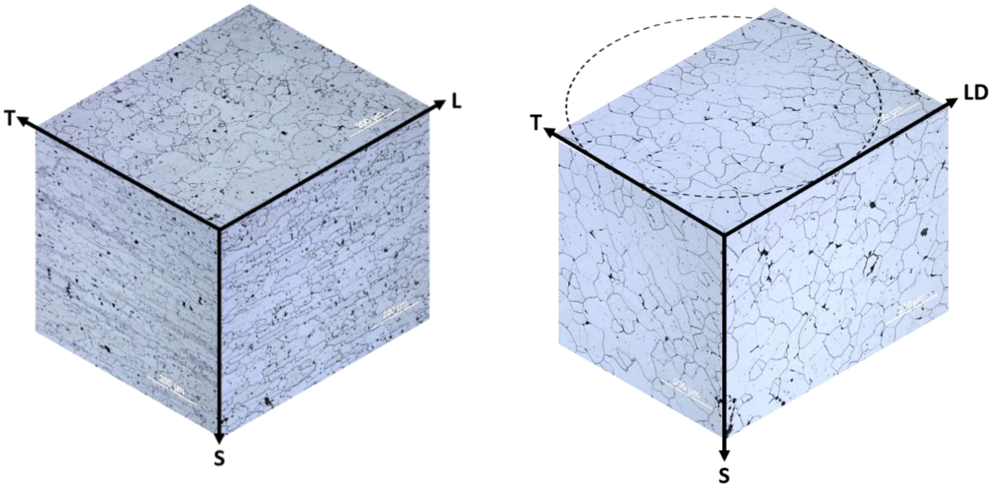

Figure 4-2: Orthogonal views of wrought-processed and CDS-processed AA7050-T6 microstructure defining the Planes of Interest

4.2.2 *Microhardness Measurements*

Microhardness measurements were made to compare the levels of strength between the two materials that were used. The wrought samples were prepared by milling through the thickness to the ¼, ½, and ¾ planes. Measurements were made on each plane along the longitudinal direction. The CDS samples were prepared by milling a tensile bar in half and measuring across the diameter and down the length of the tensile bar. All microhardness measurements were conducted using a Clemex CMT.HD microhardness tester. A 200 g with a 10 s dwell time were used, taking points at a minimum 0.1 mm apart to ensure that the indents did not affect neighboring measurements sites [26].

4.2.3 *SEM: Imaging, EDS and EBSD*

Microstructures were imaged at high magnification using a JEOL JSM-6610LV SEM. Images were taken at 500x and 1000x at a working distance of 10 mm and an energy of 10 kV to characterize the size and distribution of the large IMPs. IMPs were found by backscatter detection and then spot analyzed for elemental composition by EDS. EDS maps were constructed using Oxford Synergy system with INCA EDS X-ray micro-analysis.

The extent of grain misorientation was evaluated by Electron Back Scattered Diffraction (EBSD). Samples were polished as described above. Samples were placed in the SEM, and ideal locations were selected for EBSD mapping such that the different IMPs could be characterized. A typical map size of 600 μm × 450 μm and a step size of 1.5 μm was used to ensure sufficient data collection. Data was analyzed using the Aztec software to produce orientation maps. The data was used to show the distribution of the grain size and misorientation. Each corner of the mapped area was indented via a microhardness indenter so that the mapped area could be retrieved later for grain boundary extraction for subsequent analysis by APT. Maps were colored using inverse pole figure (IPF) coloring, and grain boundaries were colored in the following manner as seen in Table 4-2.

Table 4-2: EBSD mapping color scheme.

Grain Boundary misorientation	Color
LAGB	Black (<5°)
MAGB	Green (5°-15°)
HAGB	Red (15° - 55°) Yellow (>55°)

4.3 *Grain Boundary Characterization*

4.3.1 *Atom Probe Tomography*

Grain boundaries with a misorientation over 55° as identified by the EBSD characterization effort described above, were selected for subsequent APT sample preparation. Five APT samples were prepared for each material. Sample preparation involved Focussed-Ion Beam (FIB) milling (Zeiss Nvision 40 dual-beam SEM) to create thin foils samples, which were extracted using the following procedure. A block containing the high angle grain boundary (HAGB) was milled out and extracted with a micro-manipulator as shown in Figure 4-3.

. The block was then temporarily attached to an axially-horizontally positioned needle. The needle was removed and physically rotated on axis (typically 90°) to rotate the grain boundary orientation such that it was horizontal: positioning one grain above the other instead of beside it. A tungsten (W) protection layer was then deposited on the top. The block was trimmed down to the size of a standard atom probe lift-out needle with the grain boundary being a short distance from the new top surface of the block. The trimmed block was re-attached to the manipulator, and five segments of the block were attached to pre-sharpened silicon (Si) micro-tip posts via W deposition. The blocks were trimmed to cone-shaped needles by an annular milling pattern using a 30 kV ion beam at 40 pA. The final tip shape was achieved by a gentle milling using a 10 kV ion beam at 80 pA, which was scanned rapidly over the tip until the desired distance of 50 nm from the tip to the grain boundary was attained. The final needle tips were then attached to pre-sharpened Si micro-posts via W deposition.

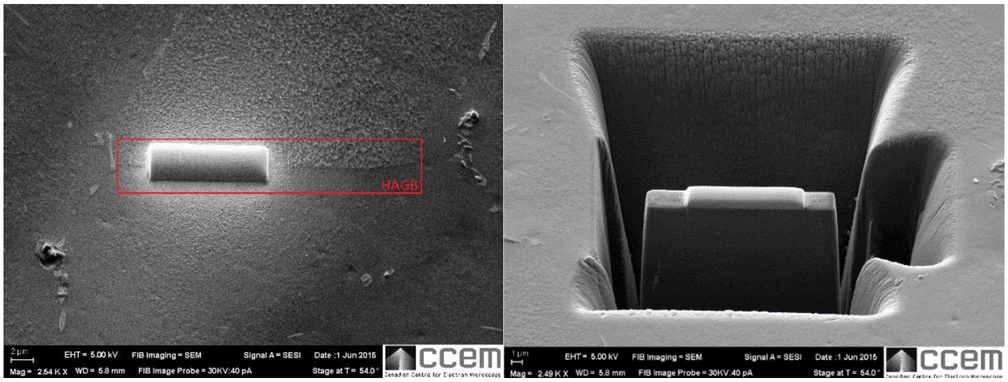

Figure 4-3: (a) W cap over selected a HAGB in the CDS material (b) FIB trenching around a HAGB in the CDS material.

APT tips were analyzed using a Cameca local electrode atom probe (LEAP) 4000X HR, operating in the laser-pulsing mode with a UV laser (355 nm wavelength). The efficiency of the atom probe was approximately 36%. Laser pulses of 50-65 pJ were used, at a pulse rate of 200-250 kHz. An evaporation rate of 0.005-0.015 atoms/pulse was maintained by varying a DC voltage applied to the sample (typically 2-9 kV). Tips were kept at a base temperature of 43.4 K, with analysis occurring under ultra-high vacuum ($3\text{-}5 \times 10^{-11}$ torr). Data was reconstructed using the Cameca integrated visualization and analysis software (IVAS 3.6.6) and established reconstruction algorithms [27]. The reconstructions were spatially calibrated using inter-plane spacing values, measured at identifiable crystallographic poles. The widths of PFZs were measured and compared. Grain boundary precipitates were compared in size, chemistry. Through the use of proxigrams η′ density in the bulk was compared.

4.3.2 *Intergranular Fracture and Auger Microscopy*

Two Charpy V-notch samples of each material were cooled with liquid nitrogen and fractured, following the procedure described in the ASTM E23 standard practice [28]. Immediately upon fracturing, sample remnants were placed into a bath of ethanol to be slowly heated to room temperature to best preserve the fracture surface. One set of fracture surfaces were observed using SEM. Appropriate areas were selected where grain boundary precipitates were plentiful. Grain boundary precipitates were identified by elemental composition by use of EDS. These grain boundary precipitates were clearly seen in the secondary electron mode due to their large size and shape Elemental composition depth profiles were then conducted through the grain boundary precipitates using AES in combination with Ar ion sputtering at a rate of 40 nm/min. This was conducted using a JEOL JAMP-9500F SAM. The remaining set of fracture samples were made into working electrodes so that the OCP behavior could be recorded to give an indication of the grain boundary reactivity. Fracture surface OCP measurements are a good indicator of the electrochemical reactivity of the grain boundaries and are sensitive to the Cu content of the grain boundary precipitates [29]. A length of Cu wire was cut and attached to the opposite end of the Charpy sample with the use of conductive tape. The wire was then mounted with a plastic tube, and the sample was masked such that only the fracture surface was exposed to the solution. OCP measurements were made using a Biologic VSP-300 potentiostat and a Saturated Calomel Electrode (SCE) and placed into a deaerated 0.5 M NaCl solution at room temperature (RT). OCP transients were measured for a minimum of 1 h to achieve a steady state. One sample had to be held an additional hour to reach steady state.

4.4 *Electrochemical Characterization*

4.4.1 *Working Electrode Preparation*

Square (1 cm^2) samples of the orthogonal planes were prepared from each material and cold-mounted in epoxy. Samples were then ground to 4000 grit and etched in 1 M NaOH at 60 °C for 1.5 min. followed by immersion in HNO_3 for 0.5 min. This was done to remove the near-surface deformation layer that forms during the mechanical abrasion used to prepare the working surface [20].

4.4.2 *Polarization Measurements*

A Princeton Applied Research K0047 corrosion cell was used with an SCE and a VSP-300 Biologic Potentiostat. A 0.5 M NaCl solution at RT was deaerated for a minimum of 45 min., after which the working electrodes were immersed, and the OCP recorded for 1 h. The working electrodes were then anodically polarized potentiodynamically using a scan rate of 0.2 mV/s starting from the OCP to an applied potential of 500 mV above the OCP.This testing was used to determine E_b for each material. At least ten replicate tests were conducted to calculate the breakdown potential and ensure reproducibility.

For the potentiostatic polarization measurements, working electrodes were polarized to an applied potential of 50 mV above corresponding E_b. Two times were considered: 0.5 h (focus on initiation) and 5 h (focus on propagation). Two measurements were conducted on each orthogonal plane and current transients were recorded. After exposure, working electrodes were cross-sectioned across the exposed surface, revealing a plane perpendicular to the through thickness, mounted in epoxy, ground to 4000 grit and polished to 1 µm. The samples were then observed under LOM and images were taken.

4.5 *Cyclic Acidified Salt Fog Testing*

4.5.1 *ASTM G85 A2 Setup*

To ensure that the salt spray chamber was calibrated correctly, the chamber (Ascott 1000L) was fitted with four 80 cm^2 capture funnels to monitor the spread of the fallout rate to ensure that even distribution was achieved. Fallout was measured for 24 h. The pump speed, air pressure and angle of the atomizer were adjusted to ensure that the fog spread evenly over the area of testing. The test was repeated after adjustment to ensure that the fallout rate was within compliance.

A standardized ASTM B117 [30] continuous near-neutral salt fog test was also conducted as part of the chamber calibration. Two SAE 1008 commercial-grade cold-rolled carbon steel panels (76 × 127 × 0.8 mm) were subjected to 5 parts NaCl, 95 parts water continuous fog environment at 35 ºC for 120 h [30].

The ASTM G85 Annex 2 [31]cyclic acidified salt fog testing procedure was conducted using two flat rectangular samples of each material. A salt solution was prepared with 5 parts NaCl in 95 parts of deionized water. Acetic acid was added to the solution to ensure a pH between 2.8 and 3.0. The saturator tower was maintained at a temperature of 57±1 °C. The temperature of the exposure zone in the salt fog chamber was maintained at 49±2 °C. Air supply was kept between 69 kPa and 172 kPa. To maintain sufficient humidity, wet bottom conditions were maintained where at least 25.4 mm (1 in.) of the solution was kept at the bottom of the chamber. Samples were spaced evenly apart in the chamber. The chamber was fitted with four 80 cm^2 capture funnels to monitor the spread of the fallout rate to ensure that it maintained the rate determined during calibration. Samples were positioned equally around the atomizer with the exposed surface at an angle of 45° to the vertical, parallel to flow of the fog. The layout is shown in Figure 4-4: The CDS and wrought material samples were placed in the chamber along with other commercial Al alloys and experimental HPDC alloys that were undergoing the same testing.

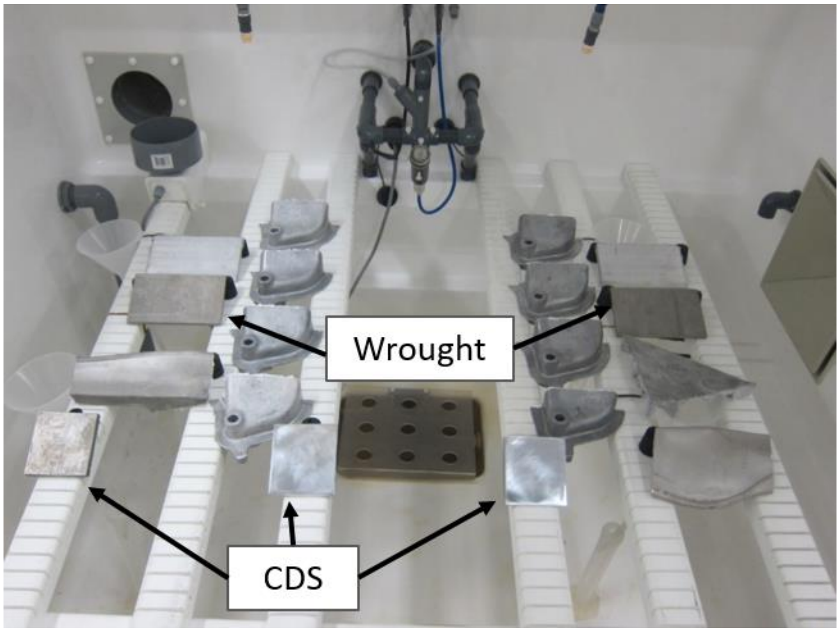

Figure 4-4: ASTM G85-A2 sample layout in the chamber

The salt fog chamber was programmed on a 6 h repetitive cycle: ¾ h fog: 2 h dry-air purge: and 3-¼ h soak at high relative humidity (95-100%). Samples were cut and polished to remove any surface impurities. Samples were then cleaned with isopropanol in an ultrasonic bath for 5 min. This was done to remove any dirt and oils from the surface that might influence the corrosion susceptibility. The sample mass was then weighed and recorded. To avoid the influence of the corrosion on edges, cut edges were masked using silicone adhesive. Samples were equally spaced in the center of the chamber to ensure consistent exposure for all samples during testing.

4.5.2 *Post-exposure Cleaning and Investigation*

Corrosion was documented weekly for the initial 4 weeks of exposure, then biweekly for the remaining 30 weeks of exposure. At the end of the test, the samples were removed and washed with water, and all silicone was removed front cut edges, and the sample was weighed.

De-scaling of the samples was performed following the procedure described in the ASTM G1 standard practice for Al alloys [32]; 50 mL H_3PO_4, (specific gravity of. 1.69), 20 g CrO_3 and reagent water to make a 1 L solution. The solution was brought to near boil (90°C to 100°C), and the samples were immersed for 5 to 10 min. If corrosion product remained, the samples were then placed into a solution of HNO_3 (specific gravity of 1.42) for 1 to 5 min. depending on the amount of corrosion left.

Once de-scaling had completed the samples were weighed again, and the weight loss per cm^2 for each was calculated. The samples were photographed and then were cross-sectioned across the exposed surface, revealing a plane perpendicular to the through thickness. It was then mounted in epoxy, ground to 4000 grit and polished to 1 µm.

The as-polished cross-sections were then observed using LOM and gauge thickness loss was measured. Gauge loss was calculated by finding the difference between the nominal thickness before corrosion and the thickness measured in LOM to quantify the extent of the corrosion. As seen below in Figure 4-5: “d” the gauge thickness lost to general corrosion can be measured by comparing the final thickness to the original after acid cleaning. A pitting factor was then calculated by measuring the depth pits in cross section and dividing by the “d”.

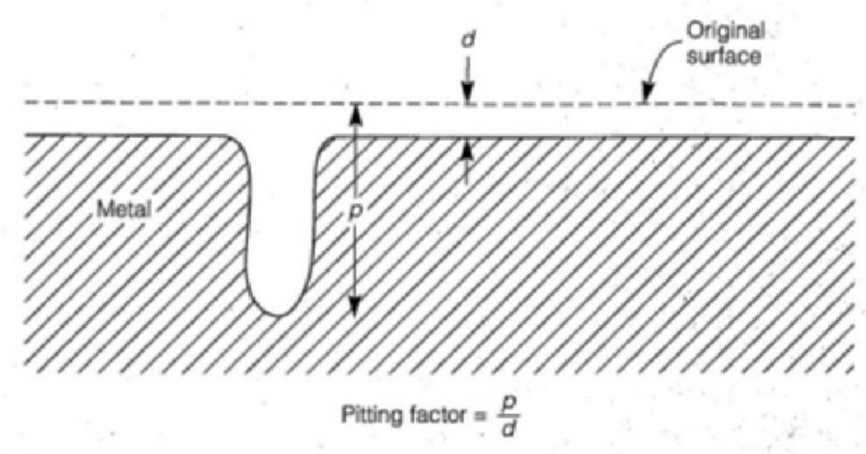

Figure 4-5: Schematic diagram to define pitting factor p/d. [33]

Chapter 5: **Results**

5.1 *Wrought Material Characterization*

5.1.1 *Microstructure*

Images of the typical wrought microstructure observed for each unique (orthogonal) orientation of each material is shown in Figure 5-1.The wrought microstructure consisted of highly elongated grains in the rolling direction forming a pancake-like structure. Grain size was measured using the line intercept method as described in section *Light* Optical Microscopy.

The LT plane had the largest grain size of the three orientations as grains underwent elongation in the longitudinal direction during working as seen in the LOM in Figure 5-1a. The grain size distribution calculated is shown in Figure 5-2a. The line intercept length was measured in each principle direction with a mean intercept length of 58±5 and 51±5 μm and in the rolling and long transverse directions respectively. The aspect ratio was measured to be 1.15. These lengths were calculated into ASTM grain sizes of 4.5 and 5.3 for the rolling and long transverse direction respectively. Mapping of the grain orientation in the LT plane is shown in Figure 5-1b.The grain boundary misorientation distribution is shown in Figure 5-3. This orientation had the lowest amount of high angle grain boundaries (HAGB) of about 60% and, inversely the highest amount of low and medium angle grain boundaries.

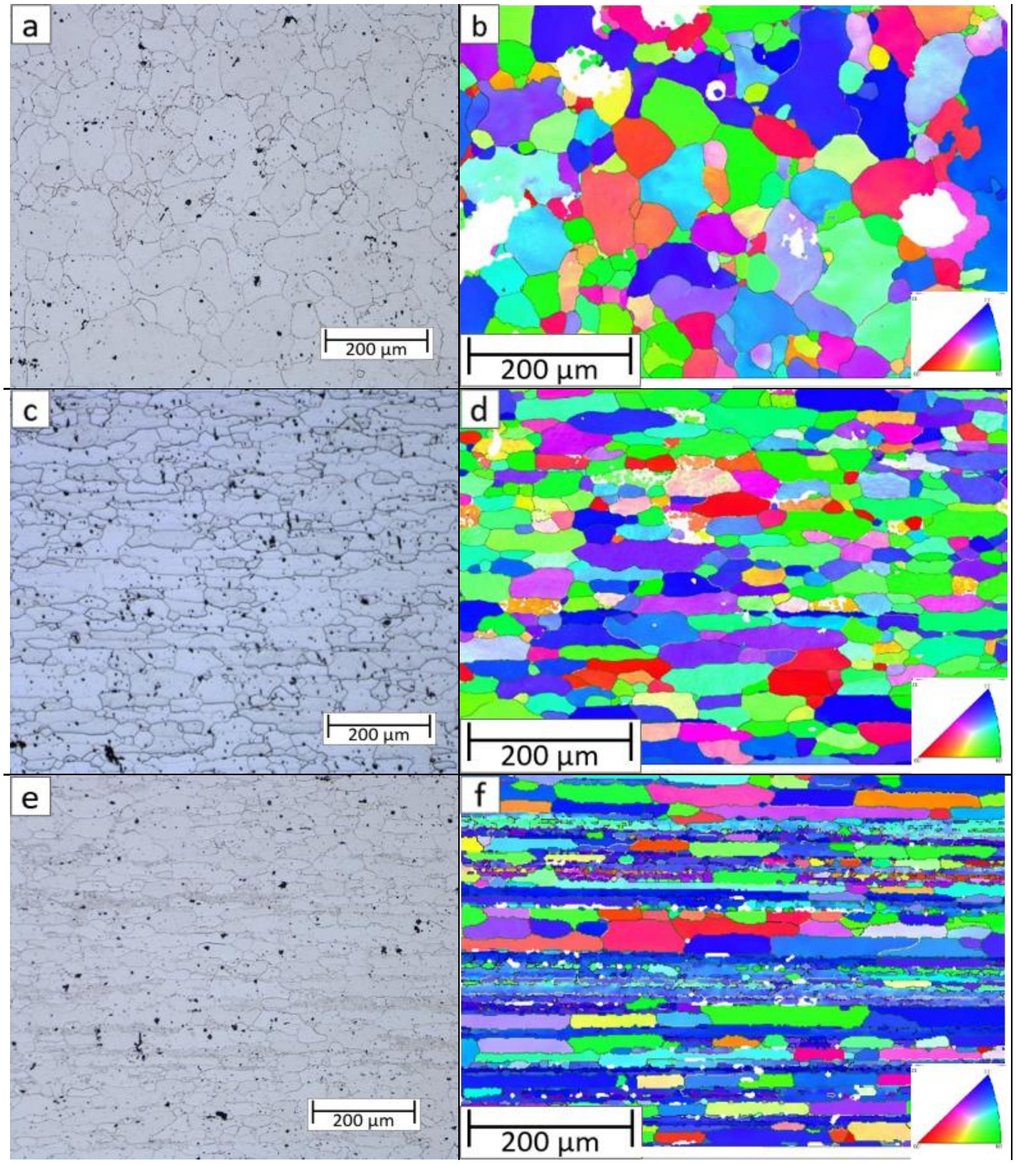

Figure 5-1: Wrought material: (a) LT plane LOM, (b) LT plane EBSD map, (c) LS plane LOM, (d) LS plane EBSD map, (e) ST plane LOM, (f) ST plane EBSD map.

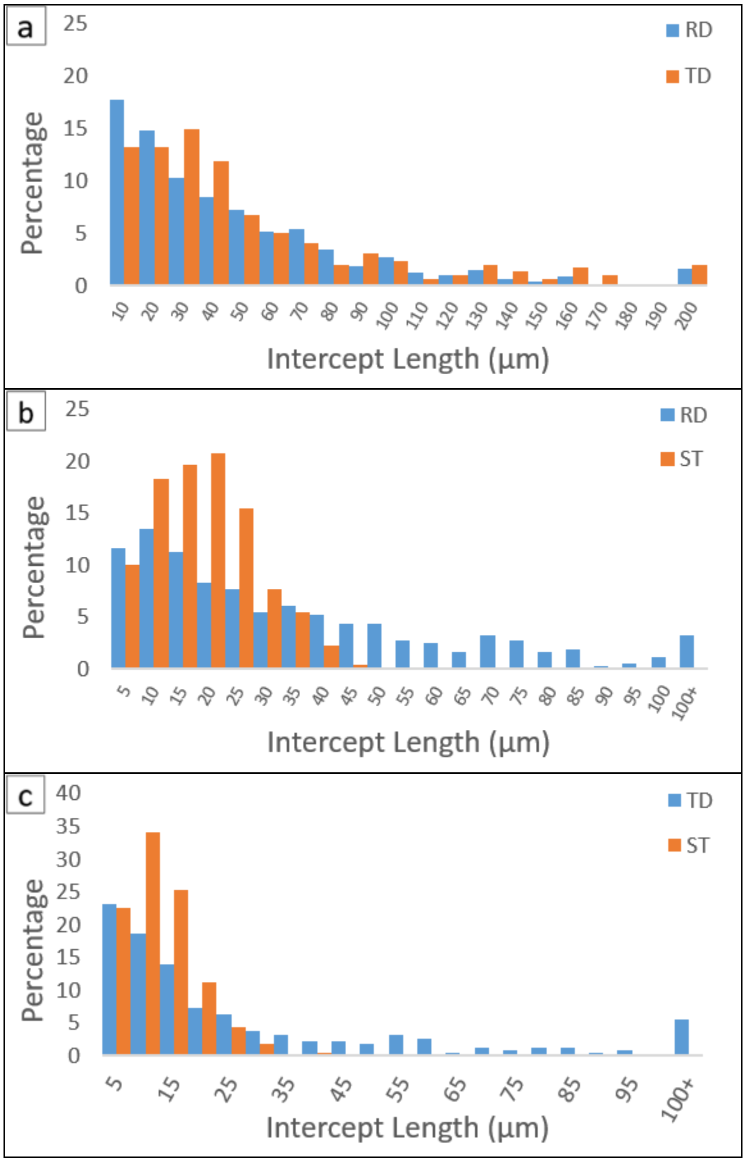

Figure 5-2: Wrought material grain intercept length distribution: (a) LT plane, (b) LS plane, (c) ST plane.

The LS plane had a grain size slightly larger than the ST plane as grains underwent compression in short transverse direction but elongation in the rolling direction as seen in the LOM in Figure 5-1b. The grain size distribution calculated is shown in Figure 5-2b. The line intercept length was measured in each principle direction with a mean intercept length of 53±3 and 13±1 μm and in the rolling and short transverse directions respectively. The aspect ratio was measured to just over 2.03. These lengths were calculated to an ASTM grain size of 6.5 and 8.6 in the rolling and short transverse direction respectively. Mapping of the grain orientation in the LS plane is shown in Figure 5-1d. The grain boundary misorientation distribution is shown in Figure 5-3. This orientation was dominated by HAGB with just over 80%.

The ST plane had the smallest grain size of the three wrought orientations as its grains underwent compression in the short transverse direction as seen in the LOM in Figure 5-1c. The grain size distribution calculated is shown in Figure 5-2c The line intercept length was measured in each principle direction with a mean intercept length of 26±3 and 10±1 μm and in the long and short transverse direction respectively. The aspect ratio was measured to just over 2.5. These lengths were calculated to be an ASTM grain size of 7.2 and 9.9 for the long and short transverse direction respectively. Mapping of the grain orientation in the ST plane is shown in Figure 5-1f. The grain boundary misorientation distribution is shown in Figure 5-3. Relative to the other planes observed, the ST plane had a high percentage of HAGB over 80%. These HAGB were mostly observed between the elongated and recrystallized grains.

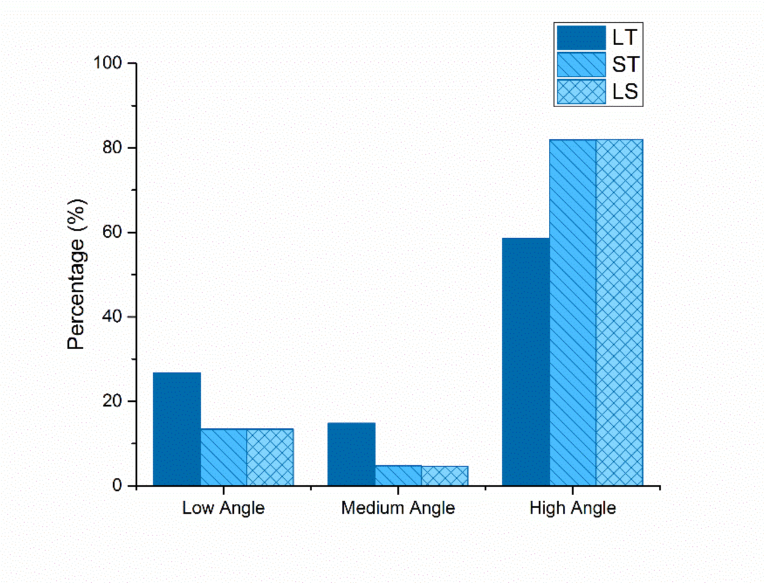

Figure 5-3: Wrought material distribution of grain boundary misorientation.

The results of the microhardness measurements are summarized in Table 5-1. The hardness was measured to 171±7 and 167±19 HV in the wrought material. There was some variance in average hardness across the through thickness of the wrought material. In both the CDS and wrought material the total average values confidence intervals were within the peak hardness of achieved by the standard wrought AA7050-T7451 (overaged) of 162 HV [34].

Table 5-1: Microhardness results of wrought material on LS plane and CDS material on the CS plane.

Hardness (HV)	¼”	½”	¾”	Top	Total
Wrought	177±6	164±9	171±5	171±4	171±7
CDS	167±19				

5.1.2 *Second Phase Particle Characterization*

SEM and EDS were conducted to characterize the size and nature of the large strengthening precipitates and intermetallics particles in the matrix. A SEM image of the LT and LS plane is shown in Figure 5-4. Figure 5-4a reveals elongated grain boundary precipitates that were aligned with the rolling direction. Figure 5-4b reveals many small Cu grain boundary IMPs and some larger Fe IMPs.

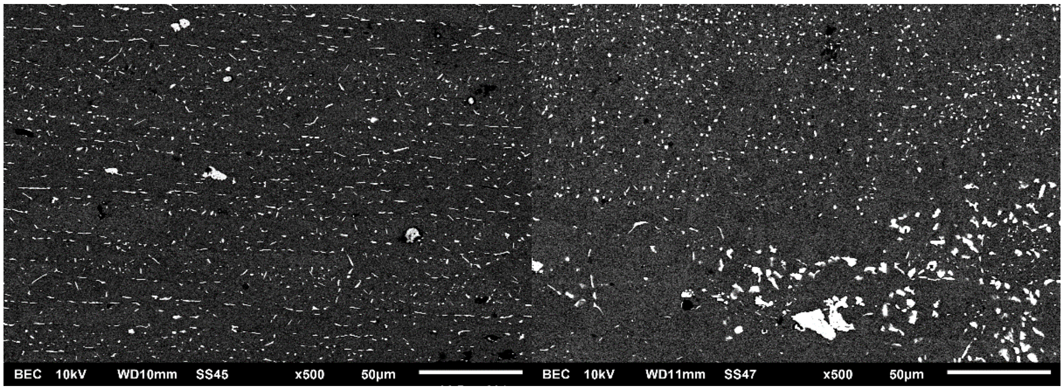

Figure 5-4: SEM imaging of wrought material: (a) LS plane 500x (b) LT plane 500x.

A higher magnified view of the LT microstructure is shown in Figure 5-5. No large Fe IMPs (over 10 µm) were found throughout the investigation, save for one the one shown at site #1 (Figure 5-5a). EDS revealed that this large intermetallic consisted of Al-Cu-Fe as shown in spectrums #1 and #2 displayed in Figure 5-5: SEM imaging of wrought material LT plane (a) Fe-rich IMP field (1000x), (b) Cu-rich IMP field (1000x) showing that the large intermetallic consisted of predominantly of Cu and Fe. The other IMPs in the microstructure consisted of Mg-Zn-

Cu as observed at sites #3, 4, 5, 8, 9 & 10. Small acicular precipitates at site 7 and 11 could not be identified due to the large interaction volume of EDS as mostly matrix was measured.

To further verify the distribution of IMPS, an EDS map was constructed as seen below in Figure 5-6. It can be seen that the precipitates contain significant amounts of Mg. Those that have elongated shaped contain large amounts of Cu as well as seen in the EDS spectra below in Figure 5-7. Fe-based IM tended to be smaller than 2 μm, circular in shape and accompanied by high amounts of Cu. Zn tended to be more evenly distributed through the microstructure.

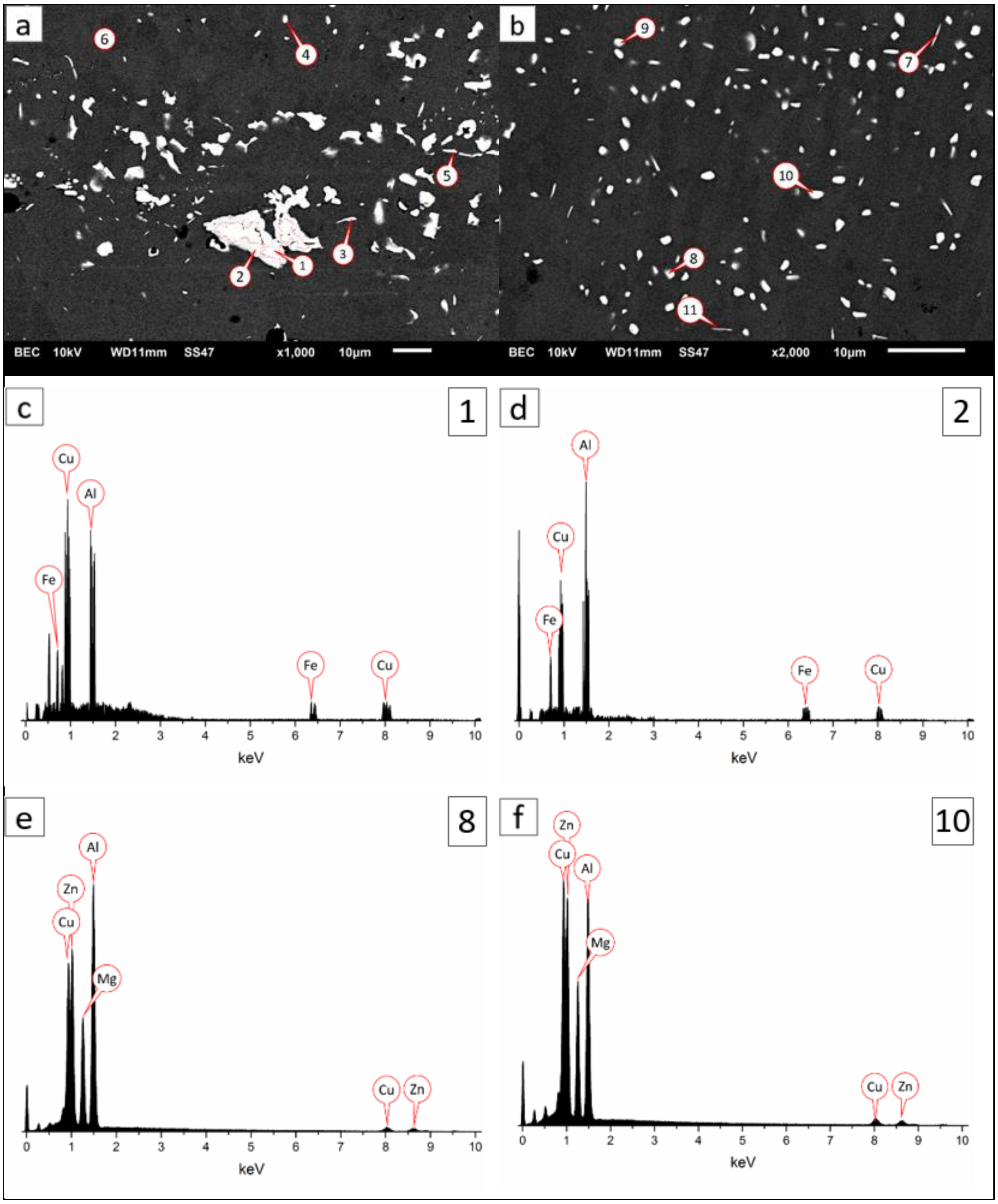

Figure 5-5: SEM imaging of wrought material LT plane (a) Fe-rich IMP field (1000x), (b) Cu-rich IMP field (1000x),(c-f) EDS results from select sites

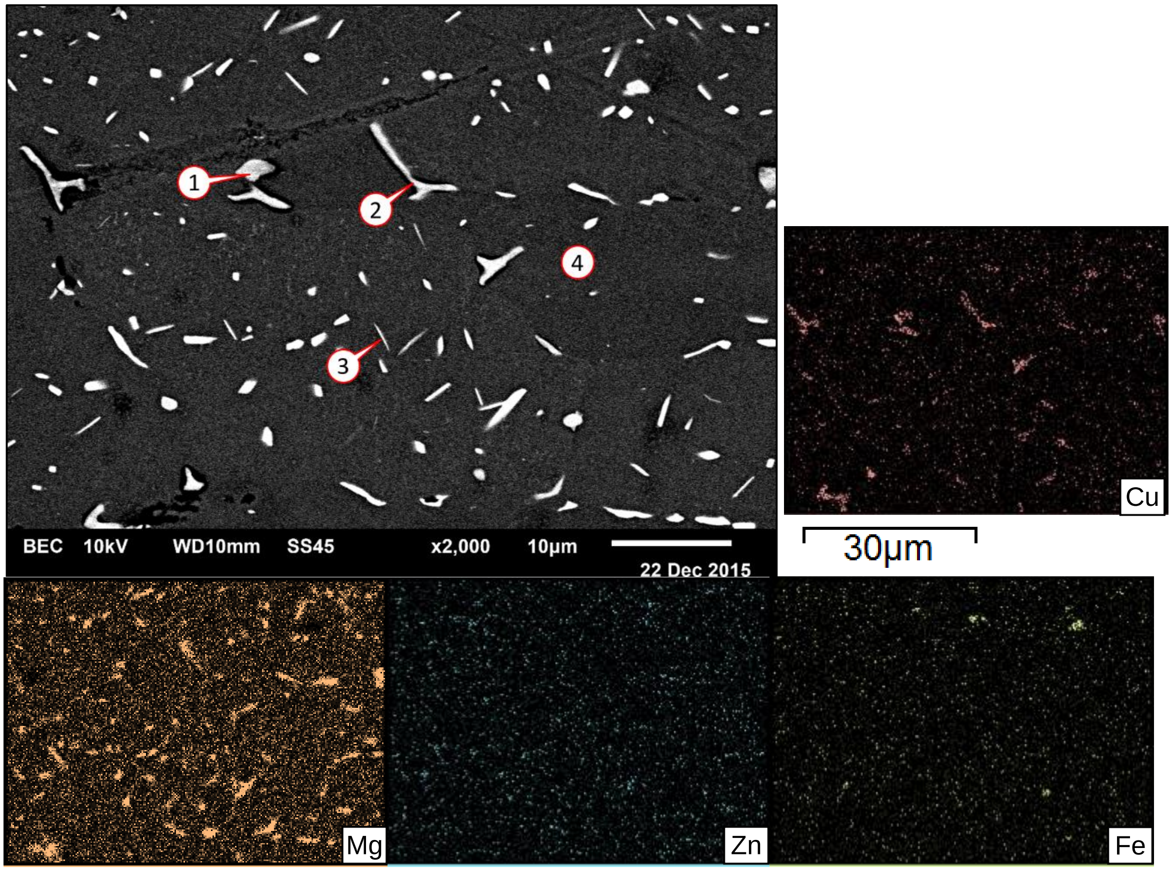

Figure 5-6: EDS mapping of strengthening precipitates on wrought LS plane 2000x.

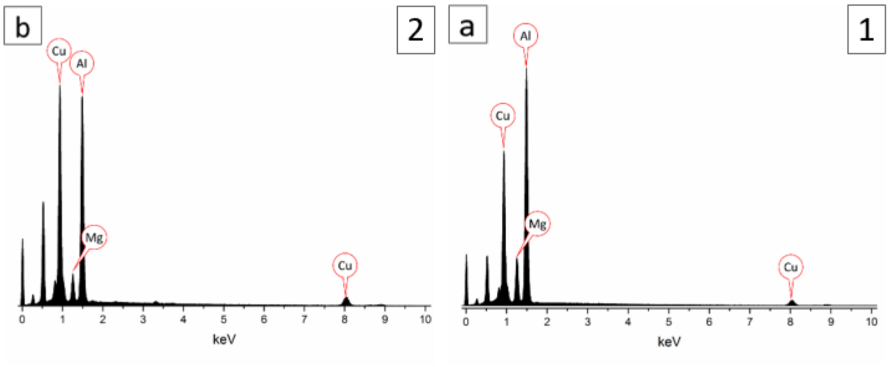

Figure 5-7: EDS results of strengthening precipitates on wrought LS plane 2000x

5.1.3 *Grain Boundary Characterization*

A typical reconstruction of an APT wrought sample through the HAGB in the wrought and CDS is shown in Figure 5-8. A 7% Zn iso-surface was applied to reveal the locations of the η $MgZn_2$ GPZ. This technique revealed the grain boundary and PFZ as well as the grain boundary precipitates. The line of dense Cu-rich precipitates shown in Figure 5-9 is a pole artifact that is common in the APT process [35].

The wrought material grain boundary tip was further investigated. 2D heat maps were created by analyzing a 5 nm slice along the Z-axis of the tip. As shown in Figure 5-9, the strengthening precipitates in the bulk were made up of primarily Zn and Mg with very little Cu. The large grain boundary precipitate contained more than 2.5% Cu and contained the majority of the Cu in the area analyzed.

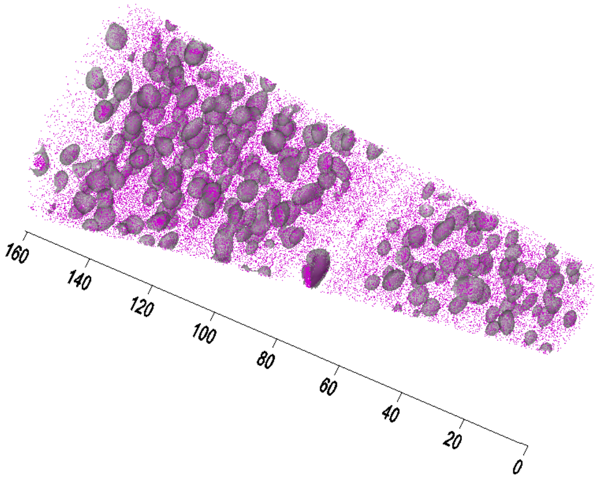

Figure 5-8: *Typical grain boundary APT tip reconstruction of HAGB in wrought material.*

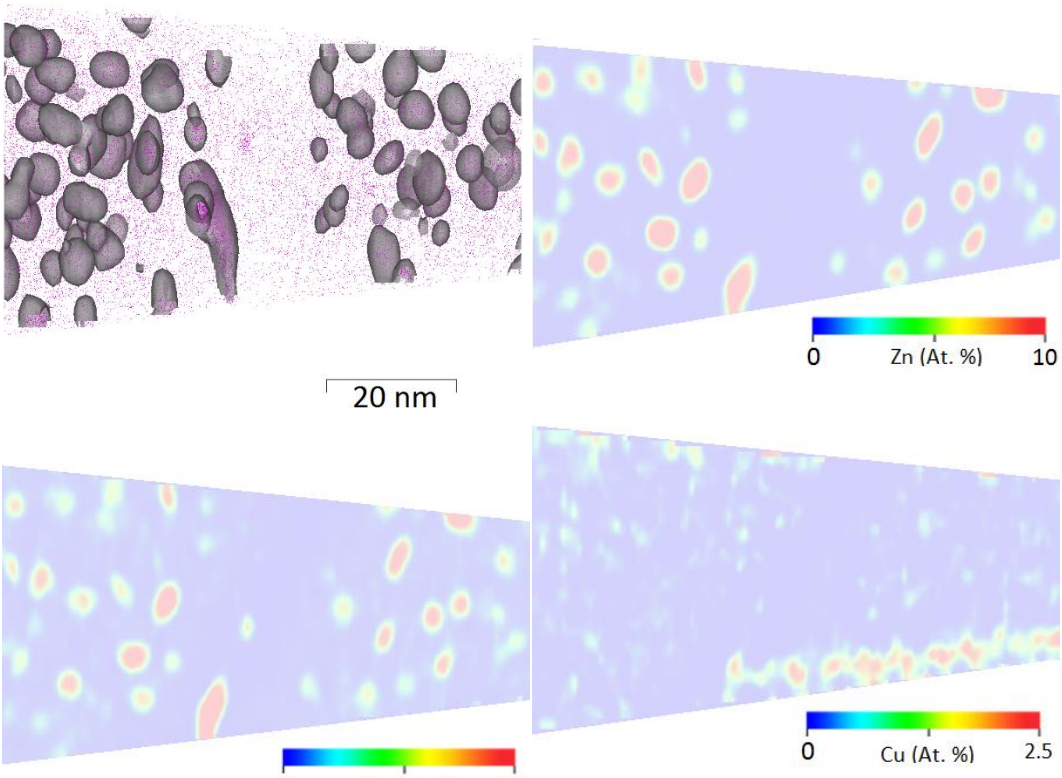

Figure 5-9: *2D heat maps across grain boundary in wrought material.*

Further investigation of the grain boundary precipitate was conducted with the use of proxigrams as shown in Figure 5-10. The surface of the precipitate was revealed by the 7% Zn iso-surfaces as shown in Figure 5-8. The grain boundary precipitate was enriched with Zn and Mg with a concomitant depletion of Al. The chemistry of the precipitate (at.%) was estimated by taking the averaged composition between 0 nm and 1.6nm resulting and found to be: 50±4% Mg, 33±2% Zn, 2.7±0.7% Cu.

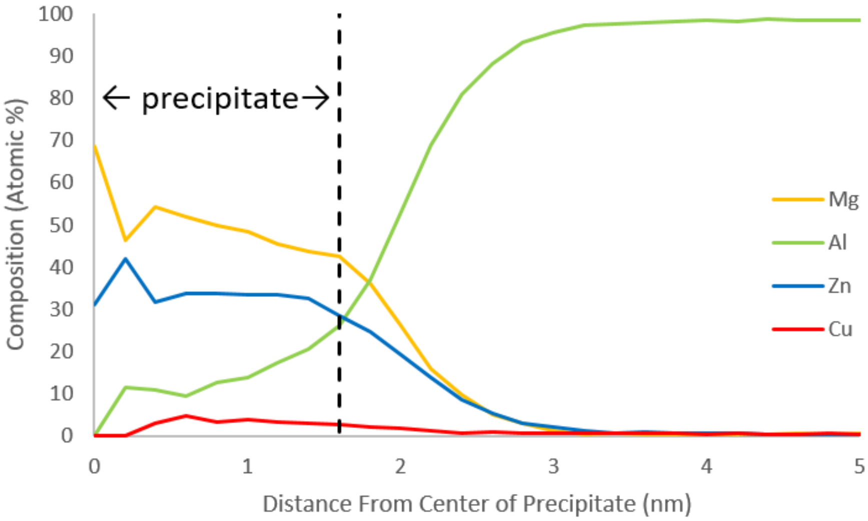

Figure 5-10: Wrought material grain boundary precipitate proxigram.

The brittle fracture surface of the wrought material was initially imaged using SEM. As shown in Figure 5-11, a high density of grain boundary precipitates litter the fracture surface. Around each exposed precipitate some ductile cup and cone features were evident. Such cup and cone features were expected since Al-alloys do not have a defined brittle-ductile transition. Nevertheless, much of the grain boundary was exposed as seen by the high density of precipitates was observed in the SE images relative to the as-polished surface. EDS mapping was conducted on selected areas as shown in Figure 5-11, which revealed large precipitates enriched with Zn, Mg, and Cu. Precipitates were elongated presumably along the grain boundaries.

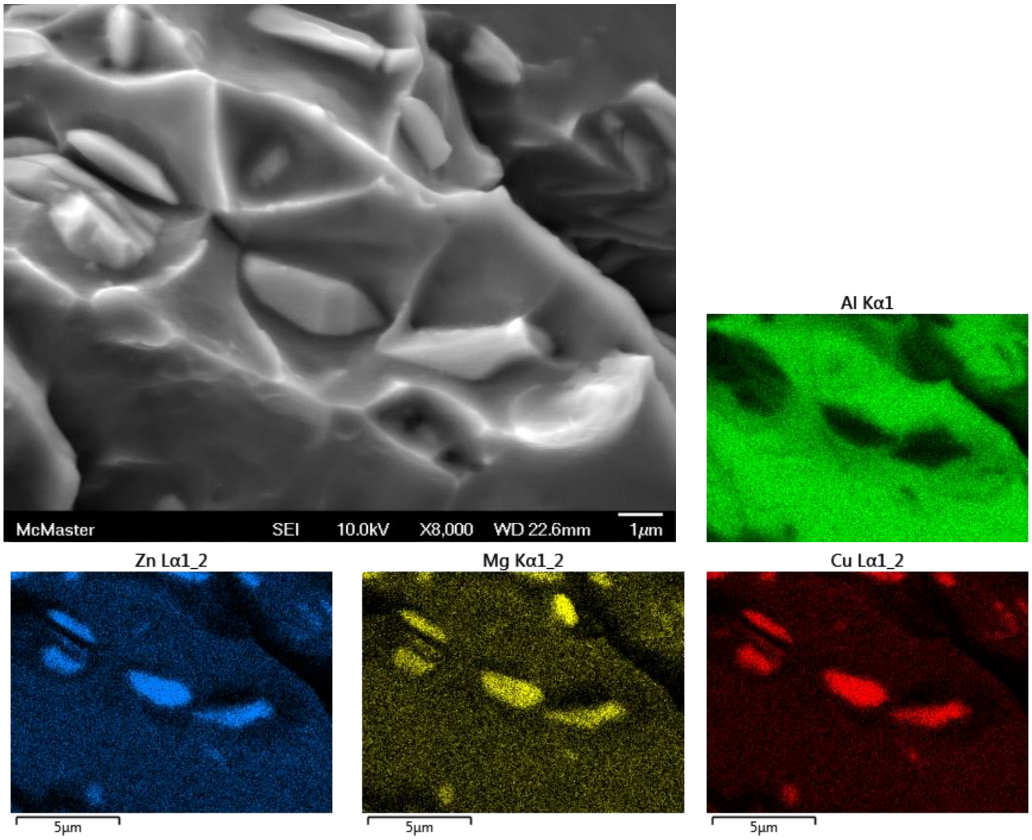

Figure 5-11: EDS mapping of large precipitates on wrought material fracture surface.

Further investigation was conducted on selected precipitates by depth profiling through the precipitate to measure the chemistry. Results of a typical depth profile are shown in Figure 5-12. Profiling revealed a ~40 nm oxide layer on top of the precipitate. The depth profiling revealed a precipitate chemistry (at.%) of 39±1% Cu, 14±0.6% Zn, 11±0.5% Mg and 35±1.3% Al in a precipitate of about 300 μm deep.

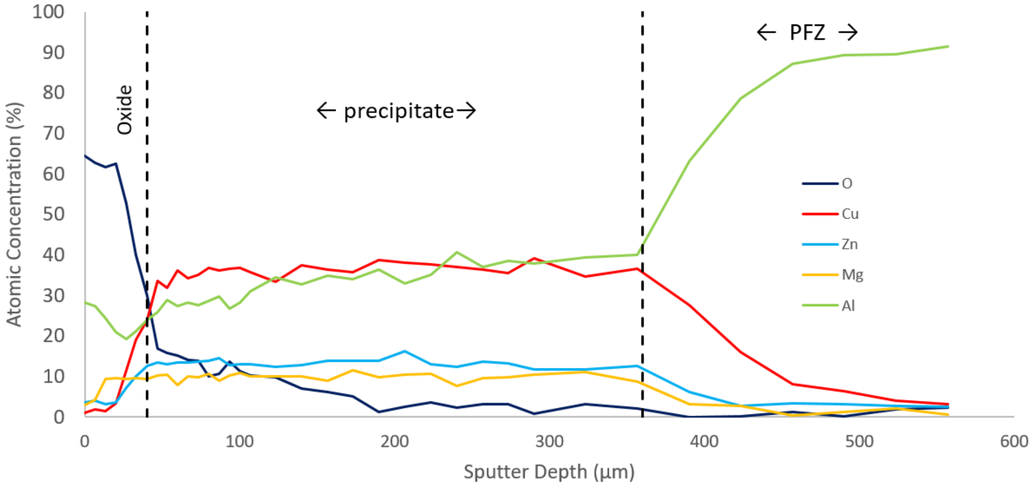

Figure 5-12: Auger depth profiling through wrought material grain boundary precipitate on fracture surface.

5.2 *CDS Material Characterization*

5.2.1 *Microstructure*

The CDS had a highly consistent, equiaxed microstructure as revealed by LOM is shown in Figure 5-13a. The CS plane had a consistent grain size that is highly equiaxed. The grain size distribution is shown in Figure 5-14b. Line intercept length was measured in each principle direction with a mean intercept length of 23±1 and 22.5±1 μm and in the X and Y direction respectively. The aspect ratio was measured to 1.04. These lengths were used to calculate an ASTM grain size of 7.6 and 7.7 and in the X and Y direction respectively. Mapping of the grain orientation in the CS plane is shown below in Figure 5-13b. The grain boundary misorientation distribution is shown in Figure 5-15. This orientation had an even distribution of HAGB with 55% while the rest were mostly low angle grain boundaries (40%).

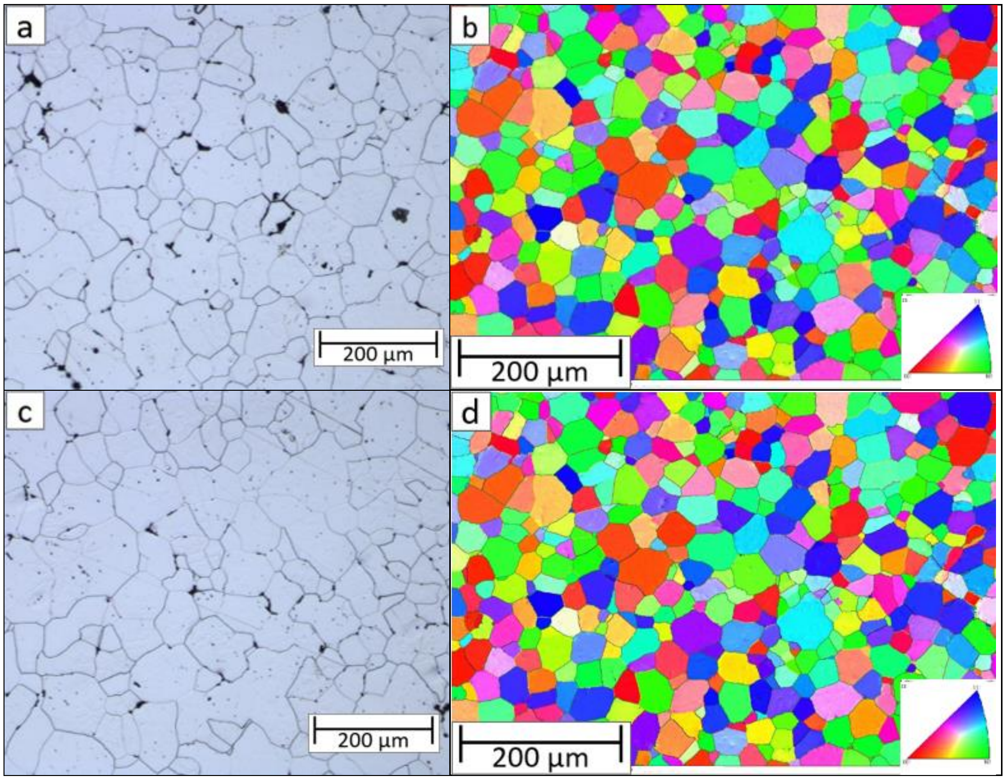

Figure 5-13: CDS material: (a) CS plane LOM, (b) CS plane EBSD map, (c) L plane LOM, (d) L plane EBSD map.

The L plane had a consistent grain size that was also highly equiaxed as revealed by LOM shown in Figure 5-13b. The grain size distribution is shown below in Figure 5-14b. Line intercept length was measured in each principle direction with a mean intercept length of 26±1 and 26±1 µm and in the X and Y direction respectively. The aspect ratio was measured to just under 1. These lengths were used to calculate an ASTM grain size of 7.2 in the X and Y direction. Mapping of the grain orientation in the L plane is shown in Figure 5-13b. The grain boundary misorientation distribution is shown in Figure 5-15. Compared with the

CS plane, the L plane had a higher distribution of HAGB with 70% with only 20% LAGBs.

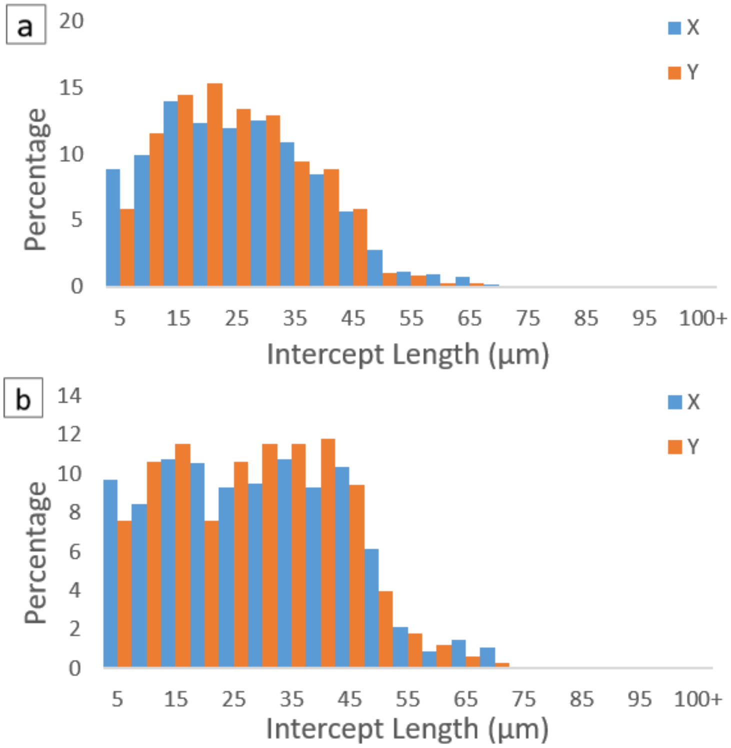

Figure 5-14: CDS material grain intercept length distribution: (a) CS plane, (b) L plane.

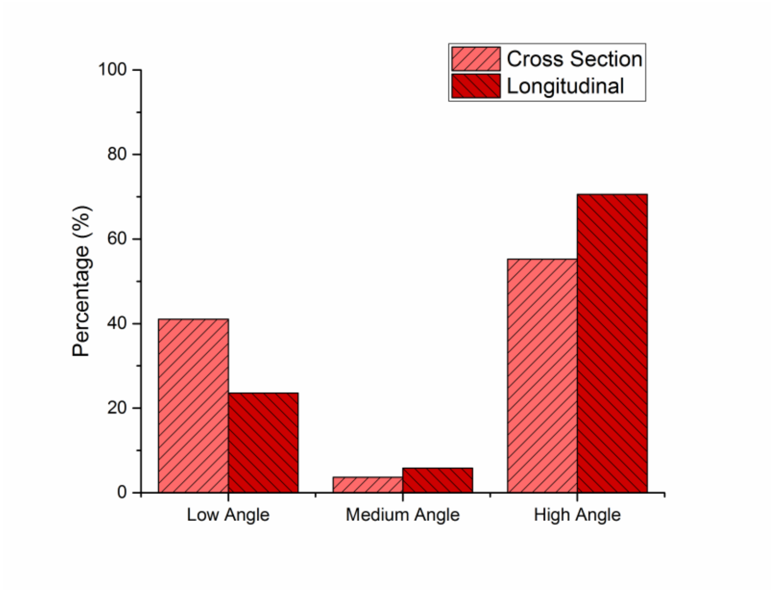

Figure 5-15: CDS material distribution of grain boundary misorientation.

5.2.2 *Second Phase Particle Characterization*

Precipitate characterization was conducted on the CDS through SEM investigation on the cross-section and longitudinal plane as seen below in Figure 5-16. There are less springing precipitates in the CDS material compared to the wrought. In the CDS material the distribution of the precipitates was indifferent to orientation with most of the precipitates relegated to the grain boundary.

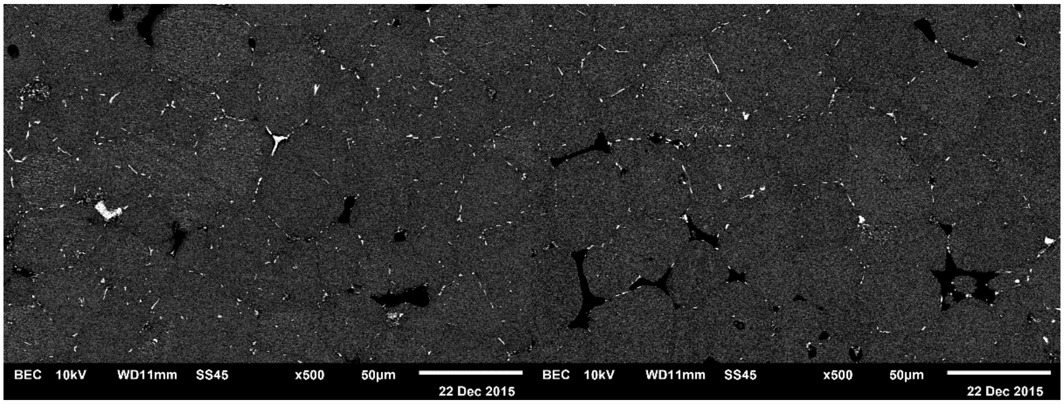

Figure 5-16: SEM imaging of CDS on (a) CS plane 500x, (b) L plane 500x.

Likewise with the wrought the precipitates were investigated with EDS, as seen below in Figure 5-17; there were more large Fe-based IM that was found at the triple points of grain boundaries then in the wrought. In

Figure 5-18 EDS spectra of sites #2,4,6 and 10 are shown. It is seen that there are Al-Cu-Fe rich IMPs at sites 6 and 10

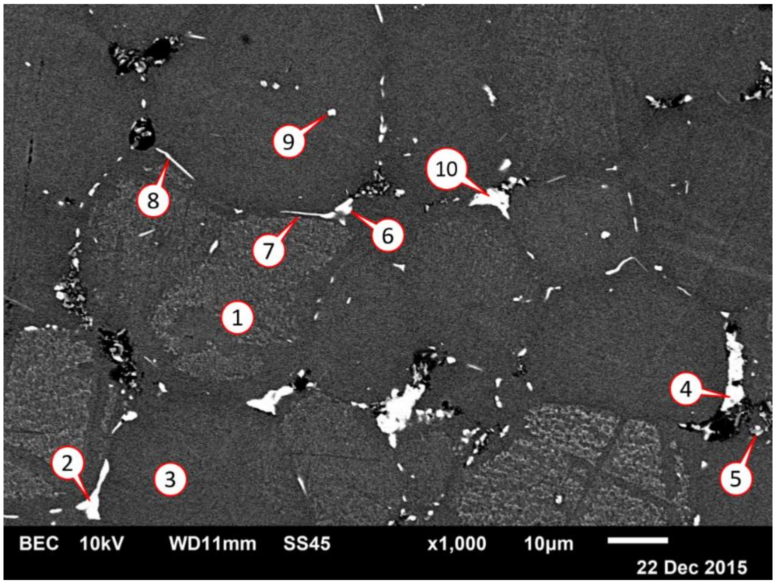

Figure 5-17: SEM imaging of Fe IMPs and precipitates on CDS CS plane 1000x.

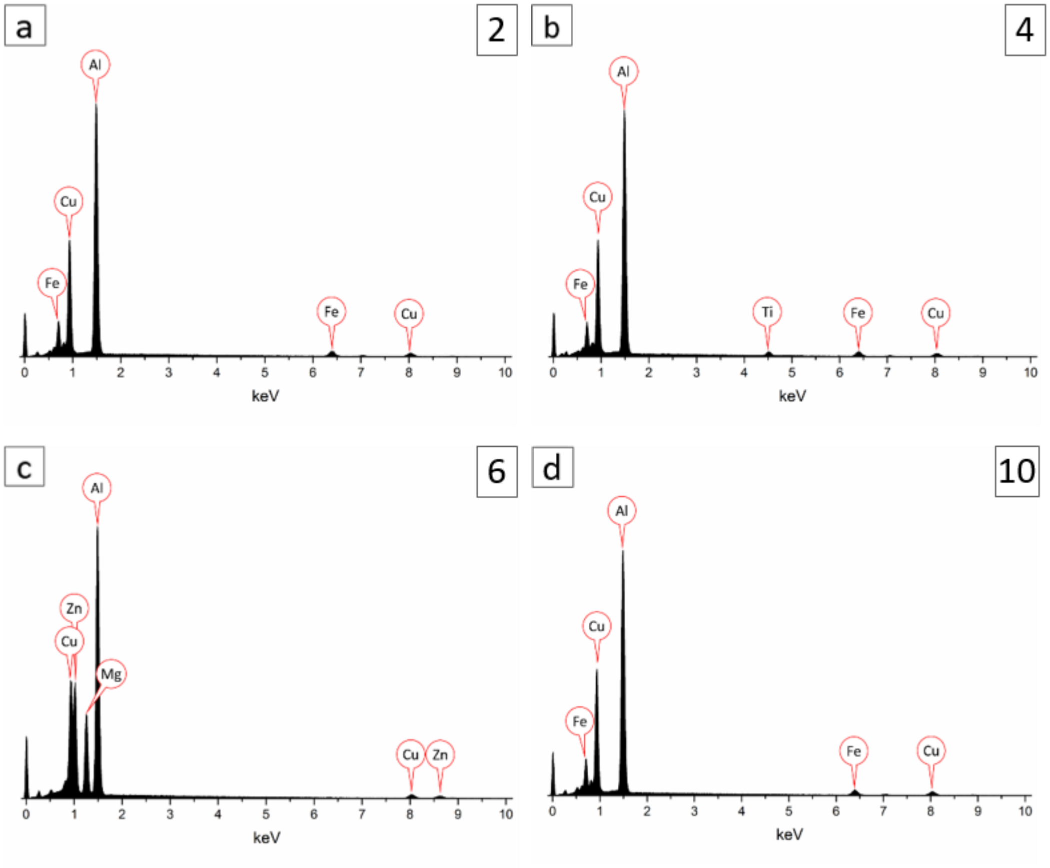

Figure 5-18: EDS results from Fe IMPs and precipitates on CDS cross-section plane 1000x

Also, with the addition of Ti, there were several Ti-based precipitates that were found with Fe IM as shown at site 4 and 5.These types of precipitates were surrounded by areas of porosity which could be caused by the issues of shrinkage due to the vast difference in chemistry with the bulk. EDS mapping in Figure 5-19 displayed the two natures of Ti-based precipitates: Site #1 Ti was surrounded by Al-Cu-Fe and was insoluble to Mg. Site #2 Ti precipitated without the presence of Al-Cu-Fe. These groups of precipitation are abundantly found throughout the microstructure on the grain boundary and sometimes entrapped in the grain as seen at site #9.

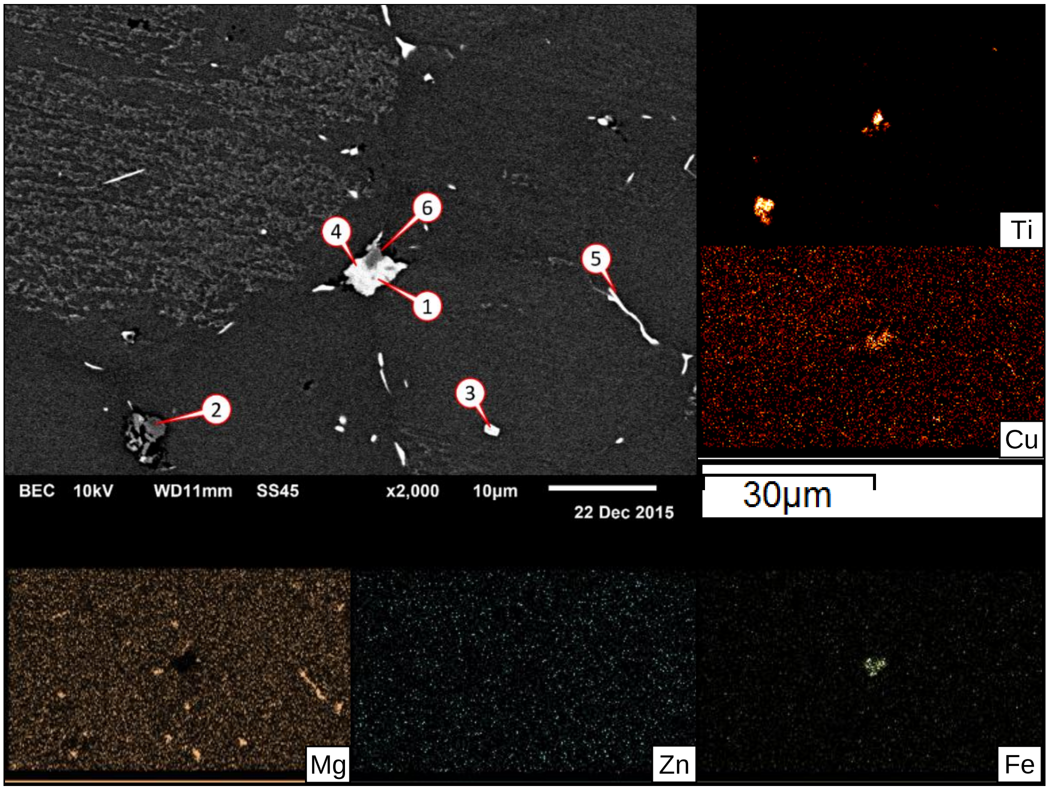

Figure 5-19: EDS mapping of Ti IMPs on CDS cross section plane 2000x

5.2.3 *Grain Boundary Characterization*

A typical reconstruction of an APT sample through the HAGB in the CDS material is shown in Figure 5-8. A 7% Zn iso-surface was applied to reveal the locations of the η MgZn2 GPZ. This technique revealed the grain boundary and PFZ as well as the grain boundary precipitates.

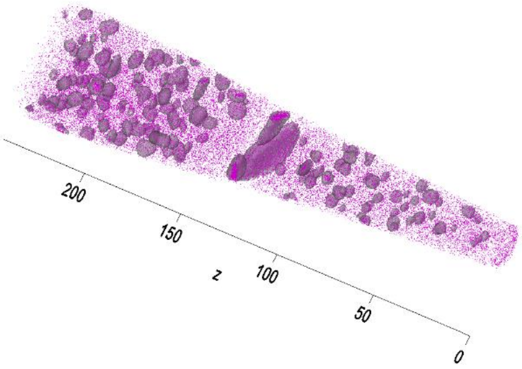

Figure 5-20: Typical grain boundary APT tip reconstruction of HAGB in CDS material.

The CDS grain boundary was in investigated by 2D heat profiles as well, the result of which is shown in Figure 5-21. The strengthening precipitates in the bulk were enriched in Zn and Mg with very little Cu. The grain boundary precipitate contained almost all the Cu in the area analyzed.

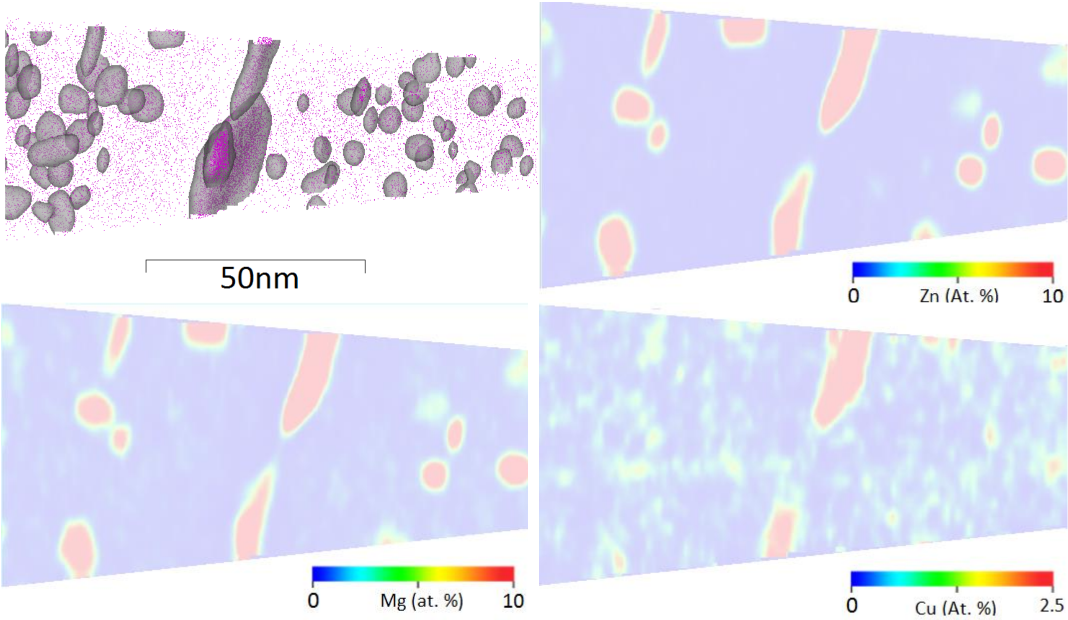

Figure 5-21: CDS material 2D heat maps across the grain boundary.

Proxigram analysis of the CDS material grain boundary precipitate was used to reveal the chemistry of the precipitate. The chemistry was estimated by taking the averaged composition of between 0 nm and 1.6 nm resulting of a precipitate of 38±5 Mg, 48±6 Zn, 7±2 Cu at.%.

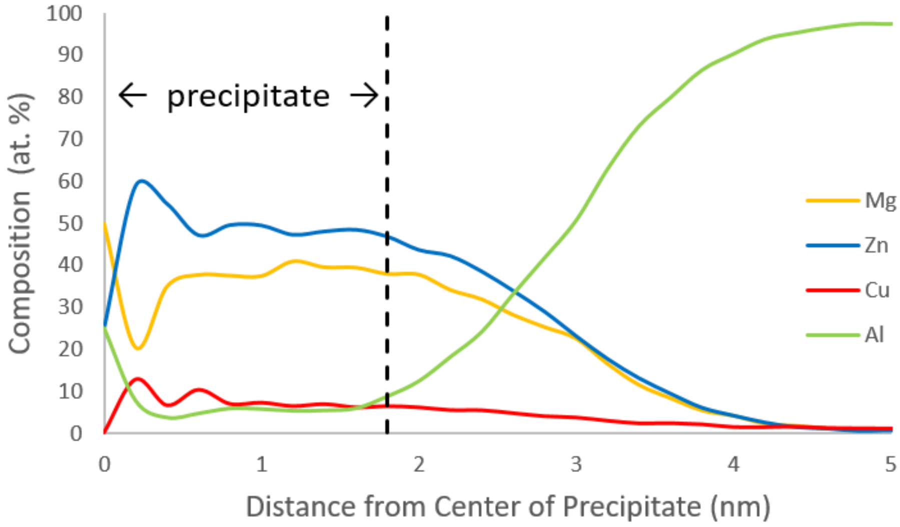

Figure 5-22: CDS grain boundary precipitate proxigrams.

Similar to the wrought material, the CDS material fracture surface was investigated as shown below in Figure 5-23. The fracture surface appeared to be more brittle as there were fewer cup and cone features seen. EDS mapping revealed similar precipitates containing high amounts of Zn, Mg, and Cu. These precipitates appeared to be circular caps that presumably sat on the grain boundaries.

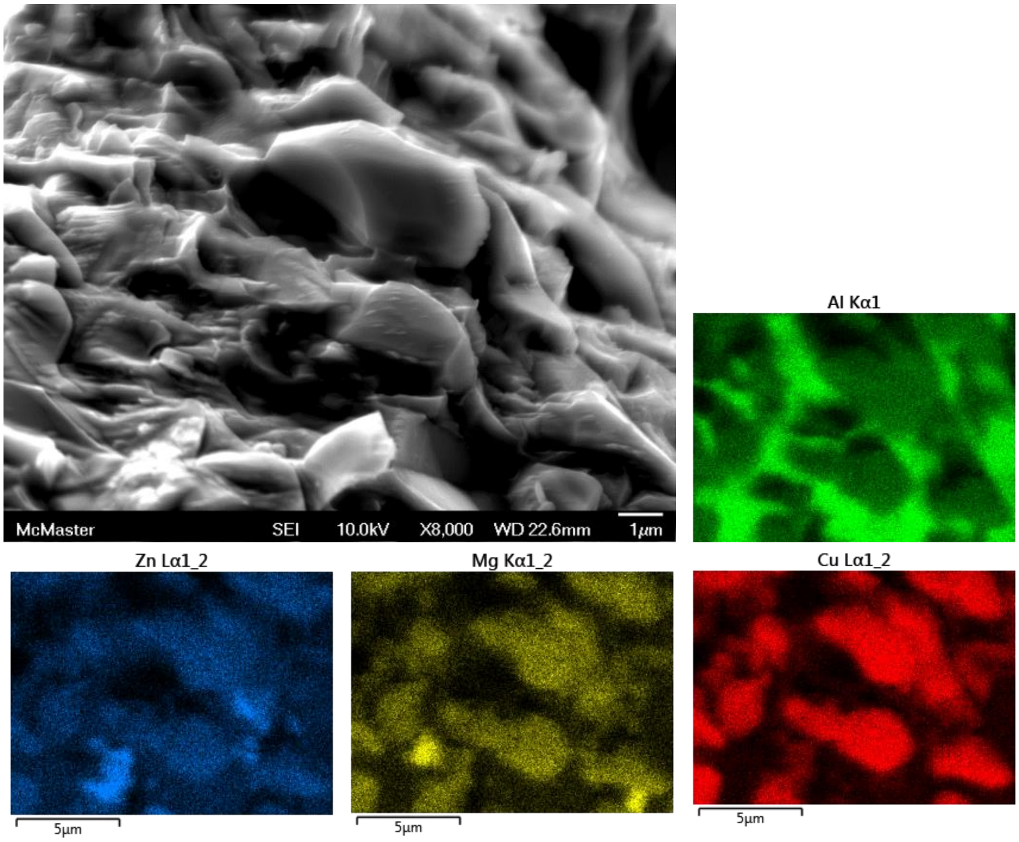

Figure 5-23: EDS mapping of grain boundary precipitates on CDS fracture surface

Depth profiling was conducted through select grain boundary precipitates. Results of a typical depth profile through these precipitates is shown in Figure 5-24. Results showed and average chemistry (at.%) of 50±0.5% Cu, 2.5±0.2% Zn, 7±0.3% Mg, and 40.5±. 0.6% Al over a precipitate of 730 µm in depth.

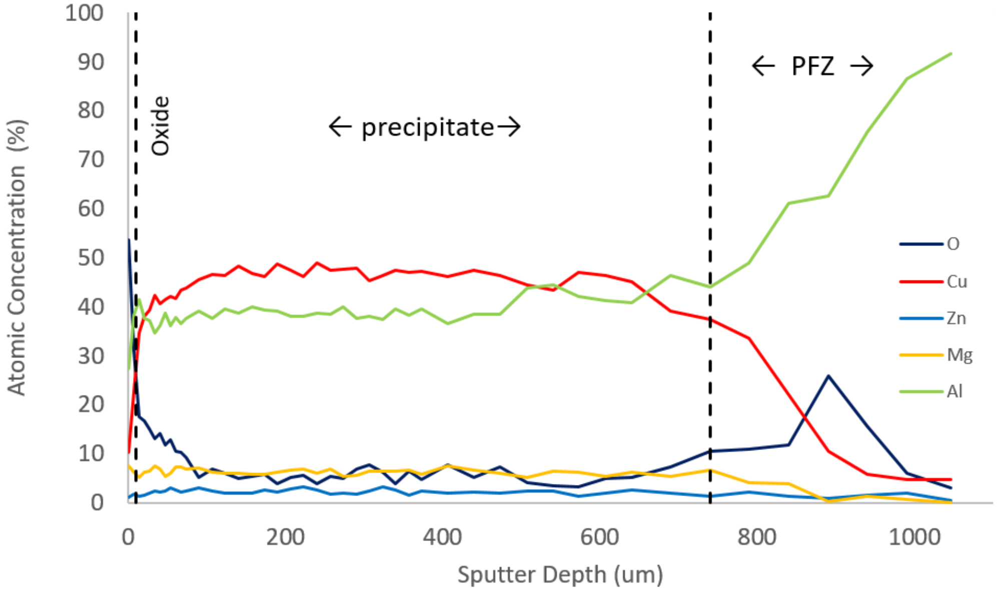

Figure 5-24: Auger depth profiling through the CDS material grain boundary precipitate on fracture surface.

5.3 *Comparative Electrochemical Behavior*

5.3.1 *Polarization Measurements*

. A typical anodic polarization for both the wrought and CDS material is shown in *Figure 5-25*. Each curve followed a level OCP reading and a breakdown potential at a higher applied voltage. Measured E_b values for each unique plane are compared in Table 5-2. The E_b of the wrought material agreed well with values published in literature [20].

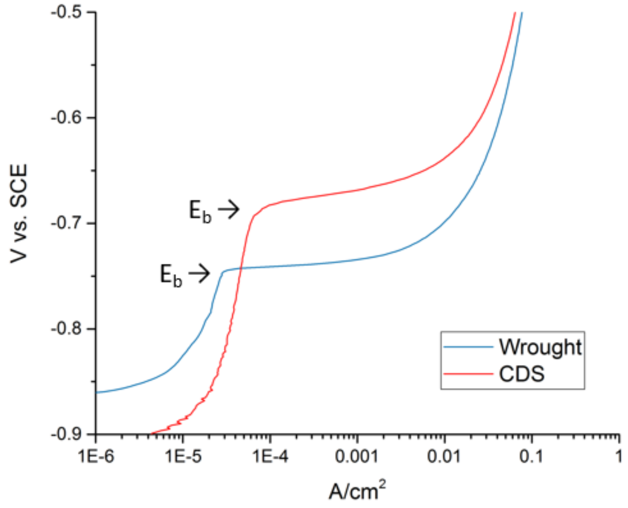

Figure 5-25: *Anodic potentiodynamic polarization behavior of wrought and CDS material in 0.5 M NaCl deaerated solution.*

Table 5-2: Breakdown potential (E_b) statistics.

Wrought		CDS	
Plane	E_b	Plane	E_b
LT	-749±4 mV_{SCE}	CS	-694±5 mV_{SCE}
ST	-749±3 mV_{SCE}	L	-703±3 mV_{SCE}
LS	-752±6 mV_{SCE}		

5.3.2 *Potentiostatic Measurements*

Results from both materials are shown in Figure 5-26. Short-term (½ h) tests provided insight on the initiation stage of the localized corrosion: It is seen that localized corrosion initiated as IGC on the wrought material surface whereas it initiated as pitting corrosion on the CDS material surface. The short-term test left many areas on the CDS surface in a the pristine condition with little or no corrosion, while some localized areas had pitting up to 50 μm in depth.

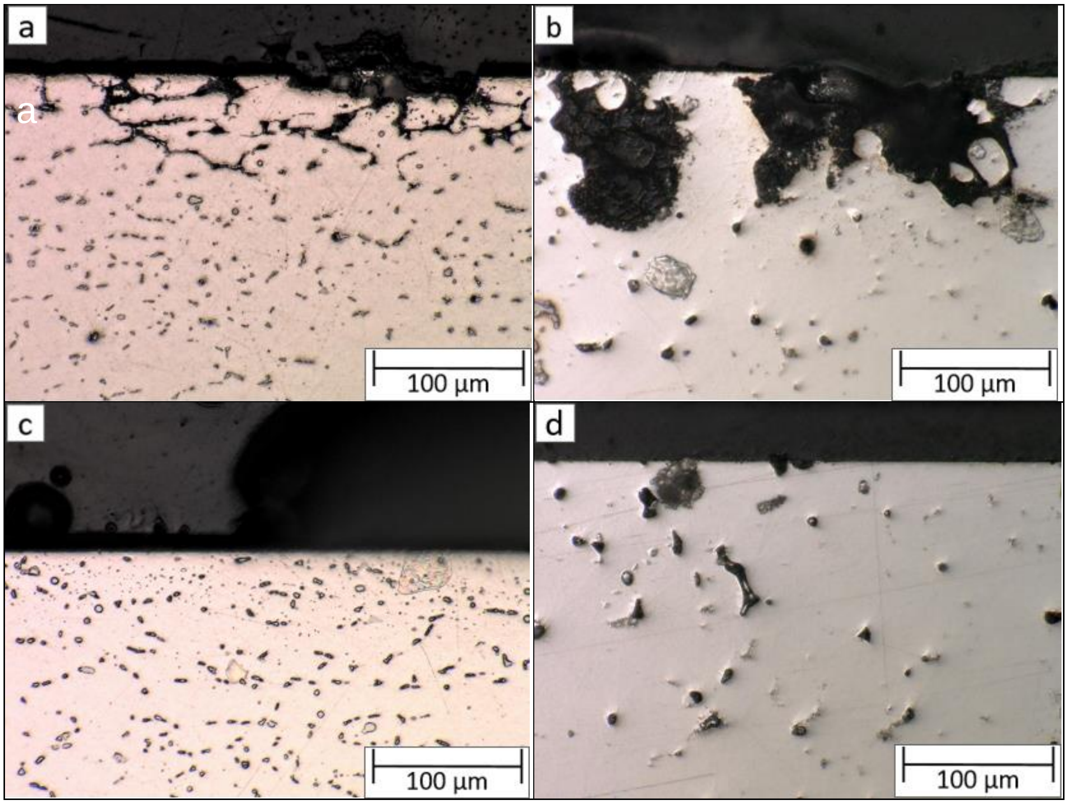

Figure 5-26: LOM of cross-sections of samples corroded via short term potentiostatic polarization testing: (a) wrought material (LT plane) after ½ h (b) CDS material (L plane) after ½ h (c) pristine surface wrought material (LT plane) ½ h. (d) pristine surface on CDS material (L plane) after ½ h.

The long-term (5 h) tests shown in Figure 5-27 provided insight on the propagation stage of the localized corrosion. The IGC that initiated on the wrought material surface continued to propagate through the thickness as IGC to a depth of 150-250 μm. In contrast, the pitting corrosion that initiated on the CDS material surface transitioned into a mixed mode of pitting and IGC with some grain lift-out. Some areas remained in the pristine condition, while some other areas were attacked down to a depth of 250 µm.

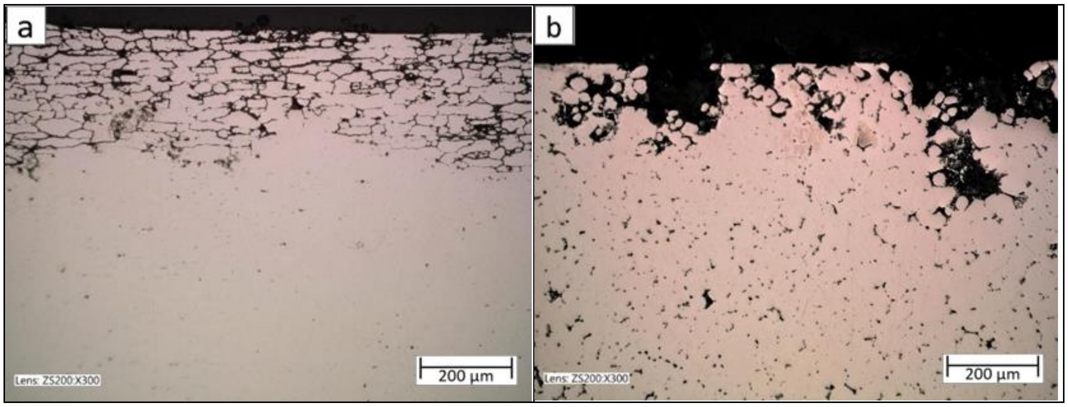

Figure 5-27: LOM of cross-sections of samples corroded via long term potentiostatic polarization testing: (a) wrought material (LT plane) after 5 h (b) CDS material (L plane) after 5 h.

Figure 5-28 compares the propagation extent of the IGC in the two cross-sectional (ST and LS) planes of the wrought material plane. Compared to the IGC into the LT plane shown in Figure 5-27a (which showed consistent depth and uniform attack along the surface), IGC propagated preferentially along grains oriented in the rolling and long transverse directions. There appears to be selective grain attack as some of the surface areas remained in the pristine condition. This can be explained by the banding of HAGB that was observed in the EBSD examination (Section 5.1) and will be further discussed in chapter 6. Higher amounts of HAGB were seen in between layers of elongated grains and recrystallized grains. These grain boundaries have higher energy and are, therefore more prone to attack.

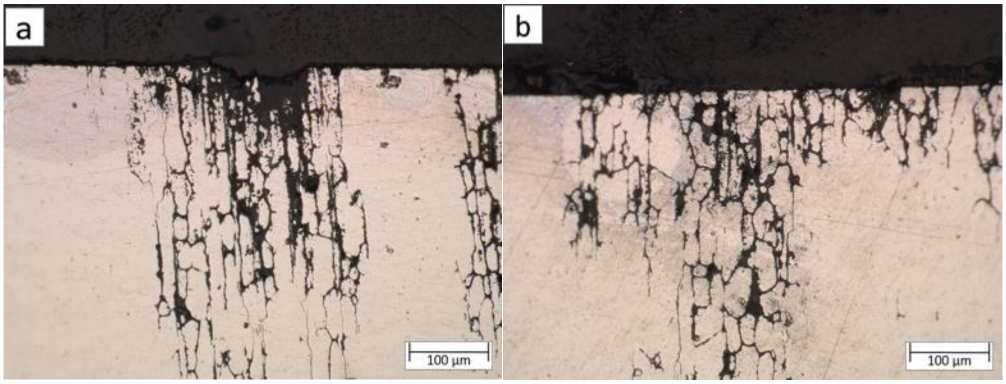

Figure 5-28: LOM of cross-sections of wrought material corroded via long-term (5 h) potentiostatic polarization testing: (a) ST plane exposure (b) LS Plane exposure.

A similar comparison was made between the two selected orientations of the CDS material. Images of cross sections of the two exposed planes are displayed below in Figure 5-29. Documented attack was similar is both orientations exhibiting localized pitting that has transitioned to the mixed mode of IGC.

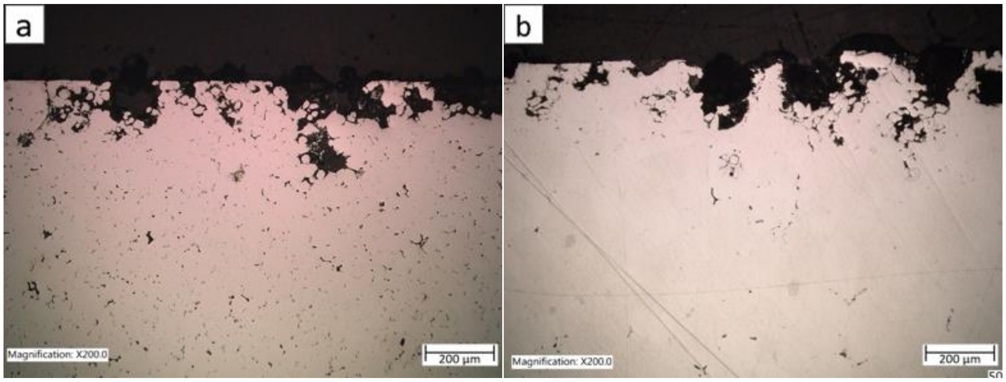

Figure 5-29: LOM of cross-sections of CDS material corroded via long term (5 h) potentiostatic polarization testing: (a) CS plane exposure (b) L plane.

Anodic current transients were recorded during the long-term (5 h) test to provide complementary information. The average current transient for each material is displayed in Figure 5-30. It was seen that the CDS material exhibited a much higher average anodic current density of 101±17 A/m^2 and 296±150 A/m^2 for the CS and L plane respectively. The wrought material had a constantly lower anodic current density. The ST plane produced the highest average anodic current density of 46±15 A/m^2, whereas the LS and LT planes exhibited an average anodic current density of 24±14 A/m^2 and 20±3 A/m^2 respectively.

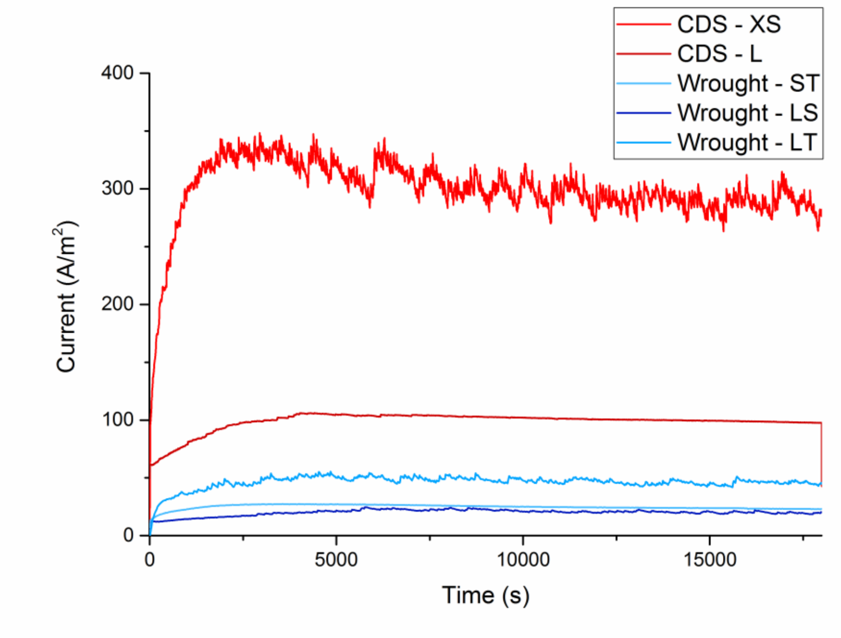

Figure 5-30: Anodic current density transients of wrought and CDS material during long-term (5 h) potentiostatic polarization testing.

5.3.3 *Bulk Grain boundary Testing*

An average of the set of three OCP transients recorded for the two materials is shown in Figure 5-31. The OCP of the wrought material fracture surface coincided with the measured E_b from the potentiodynamic polarization curve of -747±0.1 mV_{SCE} (Table 5-3).The OCP of the CDS material fracture surface was roughly 100 mV lower than the measured E_b from the potentiodynamic polarization curve of -794±0.4 mV_{SCE} (Table 5-3).

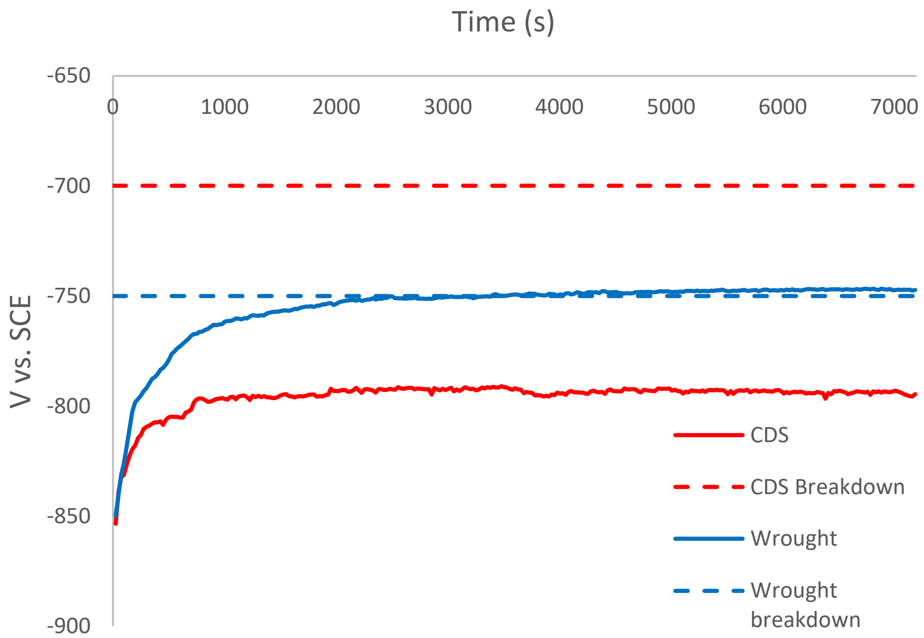

Figure 5-31: Average OCP transient of the wrought and CDS material fracture surfaces.

This OCP fracture surface behavior is best understood by initial dissolution of the anodic η based $Mg(Zn,Cu,Al)_2$ precipitates on the grain boundary followed by passivation of the remaining PFZ film with constituent secondary precipitates such as S and θ phase [29]. The stabilized OCP measurement was more anodic in the CDS material suggesting a lower Cu content at the grain boundary.

5.4 *Comparative Salt Fog Testing*

Two wrought samples underwent ASTM G85-A2 testing for a total of 30 weeks. Typical results of sample 1 are shown below in Figure 5-32. At the end of 30 weeks samples were removed, as seen in figure b the corrosion salt product is evenly built up on the surface, after acid cleaning as seen in figure c and d, the corrosion consists shallow trench like pitting that followed the rolling direction. Closer examination of figures e and f reveal that the main mode of corrosion is exfoliation with a small advancing front of IGC.

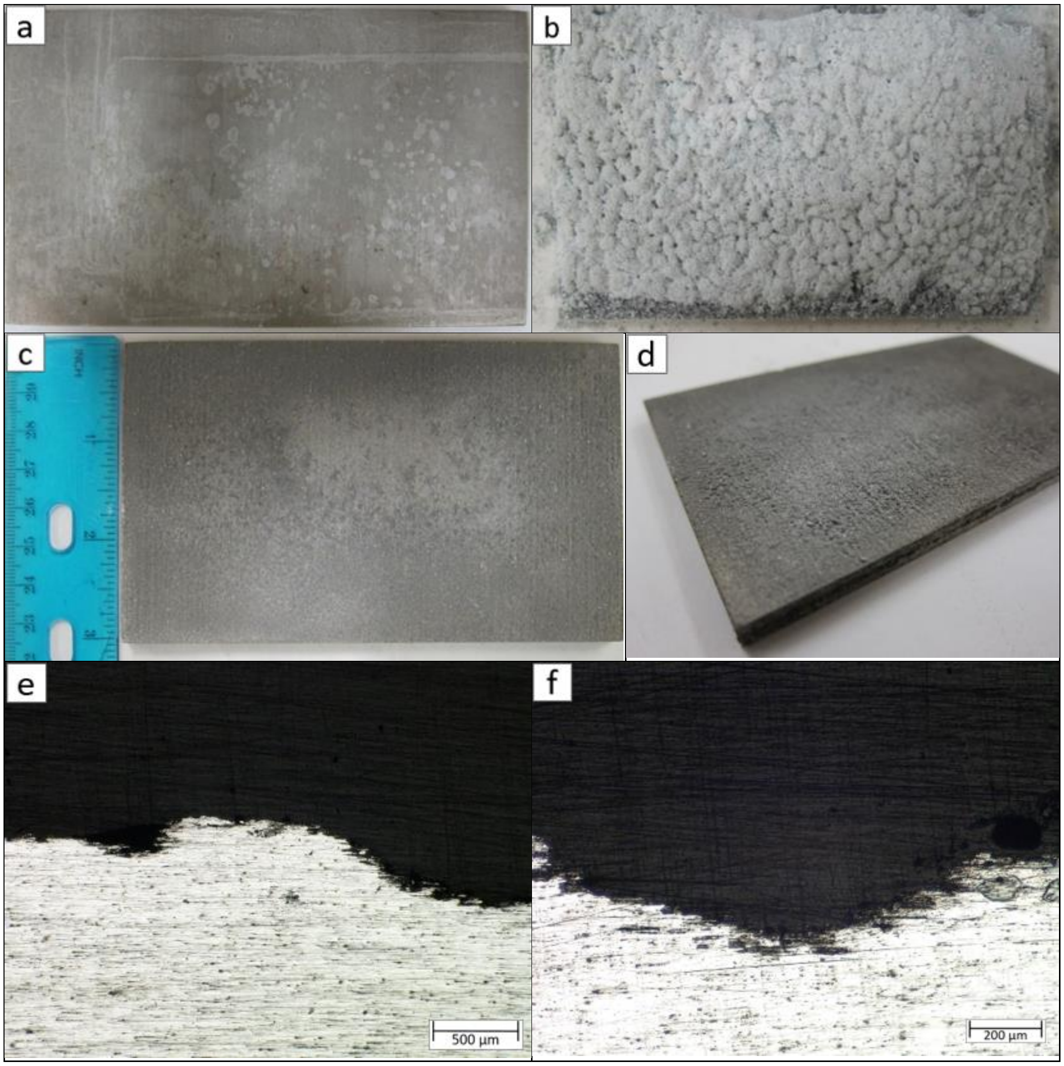

Figure 5-32: Images of the wrought material sample after ASTM G85-A2 testing: (a) unexposed sample (week 0) (b) Deposit-covered sample at week 30 (c) Acid- cleaned sample at week 30 (top-view) (d) Acid-cleaned sample at week 30 (tilted view) (e) sample at week 30 in cross-section (f) sample at week 30 zoomed cross-section.

The CDS material samples underwent ASTM G85-A2 testing for a total of 30 weeks as shown in Figure 5-33. It was seen that there was consistent pitting in each direction. Cross sections were taken from fractures that occurred during the 4th week of testing as shown in Figure 5-33e: it is seen that there was extensive pitting up to 400 µm in depth.

The bottom of the pit had evidence of IGC. While some surfaces remained in the pristine condition. Cross sections of the damaged samples seen in Figure 5-33f reveal the subsurface and undercutting pit-like nature of the corrosion which is followed by grain corrosion.

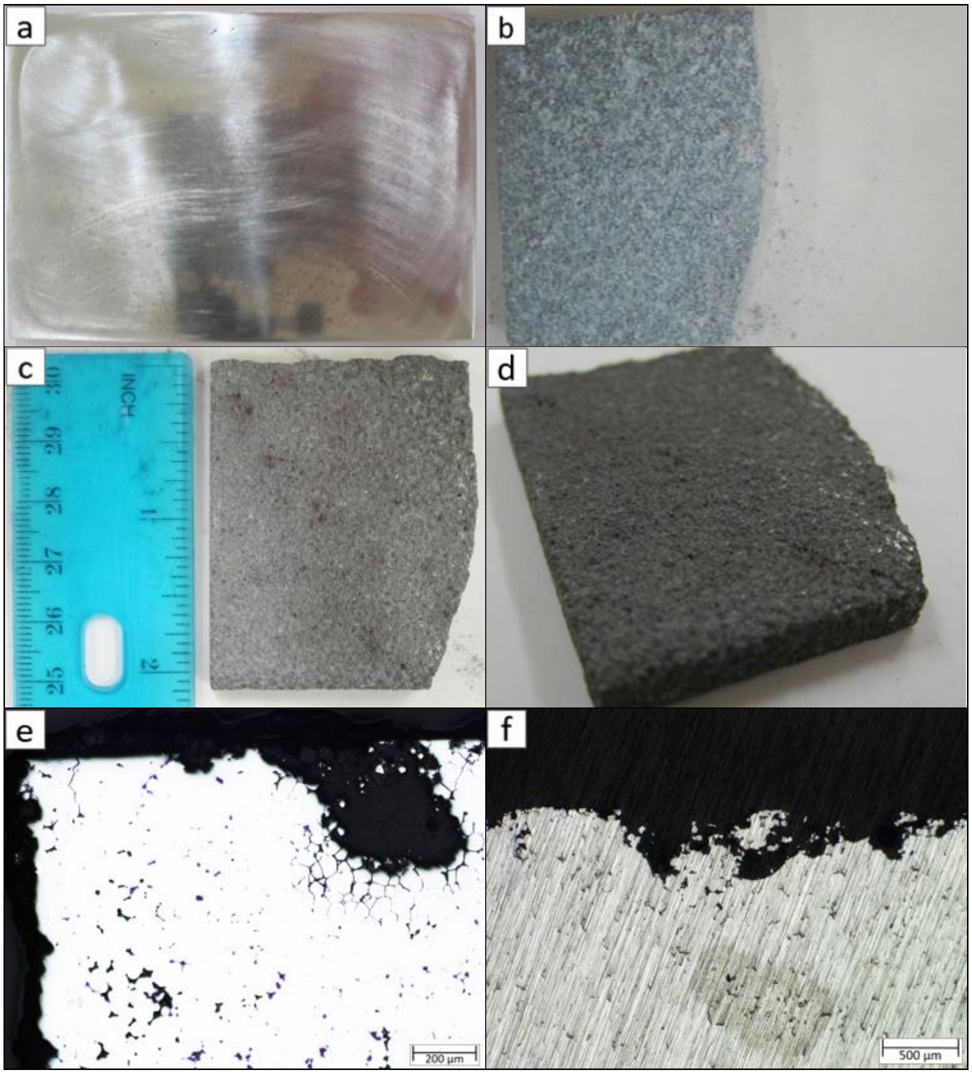

Figure 5-33: ASTM G85-A2 results CDS material (a) polished sample week 0 (b) Corrosion product at week 30 (c) Acid cleaned after week 30 (d) Acid cleaned after week 30 (e) Fracture cross section at week 3 (f)

5.4.1 *Mass Loss*

A Mass loss comparison is presented in Figure 5-34. The CDS and wrought material had a corrosion rate of 0.151 ± 0.092 mm/yr and 0.1890 ± 0.0653 mm/yr respectively Comparatively speaking, the CDS material exhibited a similar corrosion rate within the confidence interval of the wrought.

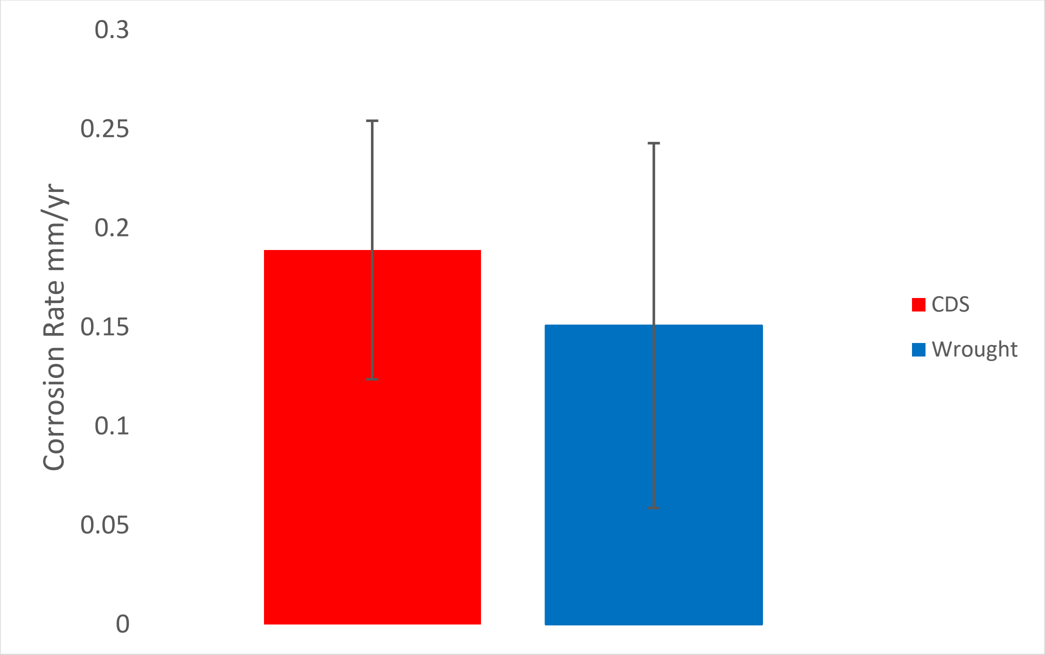

Figure 5-34: ASTM-G85 corrosion rate comparison between CDS and wrought material after the 30 week testing period.

5.4.2 *Gauge Thickness Loss*

Loss of gauge thickness was calculated by comparing the original thickness and the thickness measured of the corroded samples after acid cleaning. Results of gauge thickness lost are shown below in Table 5-3. The CDS produced an average gauge thickness loss the 95% CI of the wrought average proving to be insignificantly higher. Gauge thickness was used to estimate general corrosion “d”. Pit depths could then be measured, and an average pitting factor could be calculated. The wrought material had consistently large, wide pits about 4 times the depth of the general corrosion, while the CDS had much more vigorous pitting with some pitting deeper than 10 times the depth of general corrosion.

Table 5-3: Gauge Thickness Loss after 30 weeks of G85 testing.f6-

Material	Gauge Thickness Loss (μm)	Pitting factor (P/D)
Wrought	87±52	3.9±0.65
CDS	109±38	5.8±1

Chapter 6: **Discussion**

The results presented in the previous chapter show that the wrought and CDS processed AA7050 materials had distinctly different microstructures including differences in IMP size and distribution, Cu segregation in grain boundary secondary phase precipitates, grain structure, and grain boundary misorientation. The relative differences in localized corrosion susceptibility manifested can be directly correlated to the differences in microstructure between the two materials. This chapter ties the findings together.

6.1 *Differences in Microstructure*

The wrought microstructure had grains elongated in the rolling direction and long transverse direction. The grains had an average intercept length in each principle direction as shown in Table 6-1. It was seen that grain size measured was a ¼ of the grain size measured in other studies on similar materials [36] [37]. The aspect ratio between the longitudinal length and short transverse length was also significantly less than that in other studies of about 4.3.

Table 6-1: Grain size in micrometers (µm) in the three perpendicular directions of wrought material.

Source	Longitudinal	Transverse	Short-Transverse	Aspect Ratio
7050-T6	56 ± 3	51 ± 3	13 ± 2	4.3
7050-T7451 [37]	225	77	36	6.25
7050-T7451 [36]	232 ± 68	121 ± 36	20 ± 8	11.6

The CDS material had a completely equiaxed microstructure and isotropic properties with similar Gaussian grain size distribution in each direction, as well as no grain texture. The aspect ratio was close to 1, and the grain size is shown in Table 6-2: the CDS material had a grain size half of that observed in one of the few other studies on a CDS AA7050 material that was solutionized and annealed [2] [38].

Table 6-2: Grain size in micrometers (µm) in the two perpendicular directions of CDS material.

Source	X	Y	Aspect Ratio
7050 - T6	25 ± 1	24 ± 1	1
7050 – T4 + O [38]	55 ± 2		1

The wrought material had bands of recrystallized grains between elongated grains, which lowered the average grain size in each direction and resulted in a non-Gaussian grain size distribution. In Figure 6-1a some of the borders between elongated and recrystallized grains are noted. It was found that the bands of elongated recystalized grains contained more HAGBs as denoted in Figure 6-1b by red and yellow grain boundaries as well as along the border between the bands of elongated and recovered grains. The majority of MAGBs (green) and LAGB (black) were found on recovered grains.

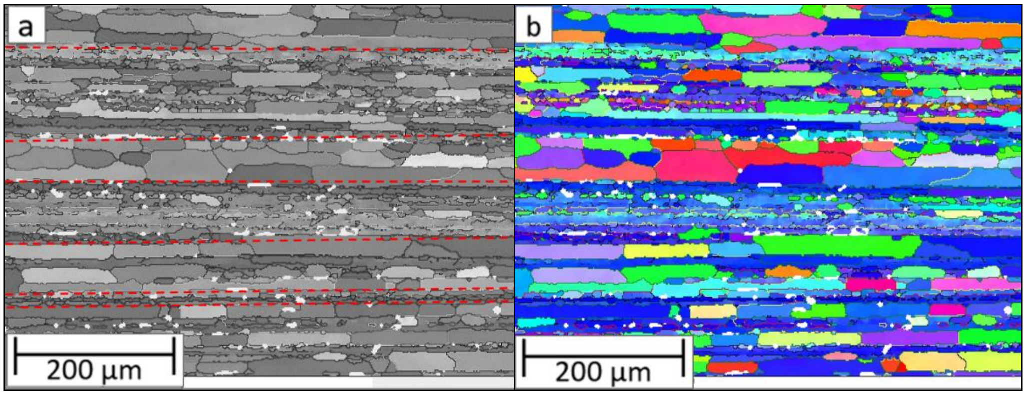

Figure 6-1: Elongated and recrystallized layers in wrought material on ST plane

A summary of the grain boundary misorientation distribution is shown in Table 6-3. In the wrought material, the percentage of LAGB was influenced by the number of recovered grains exposed. Studies by Gu et al. [39] demonstrated that sensitivity of wrought AA7050 to tempering: it was shown that additional temper heat treatments could increase the percentage of recrystallized grains and percentage of LAGB. From the corrosion perspective, reduction of HAGBs would be attractive, as HAGB contain higher amounts of surface energy and are where grain boundary precipitates are generally more abundant causing them to be more prone to IGC [40]. The CDS material displayed a similar distribution of grain boundary misorientation as the wrought LT plane. The grain boundary misorientation distribution through the microstructure though was random as seen in Figure 5-13.

Table 6-3: Distribution of grain boundary misorientation in the wrought material

Source	LAGB (%)	MAGB (%)	HAGB (%)
LT	26.7	14.8	58.5
LS	225	4.7	82
ST	13.4	4.7	81.9
7050-T6 (LT) [39]	30	15	55
CDS - CS	41	4	55
CDS - L	23	5	70

There were significant differences between the wrought and CDS material in the nature and distribution of the IMPs. In these materials, there were three main types of IMPs: Cu-rich S and θ IMPs and Fe-rich impurities. Typical wrought microstructure is shown in the through thickness in Figure 6-2: thermo-mechanical processing resulted in the even distribution of Cu-based S and θ IMPs along the grain boundaries while dispersing large Fe IMPs to sizes below 2 μm (Figure 5-6). This was generally consistent with other studies of wrought AA7xxx alloys [41].

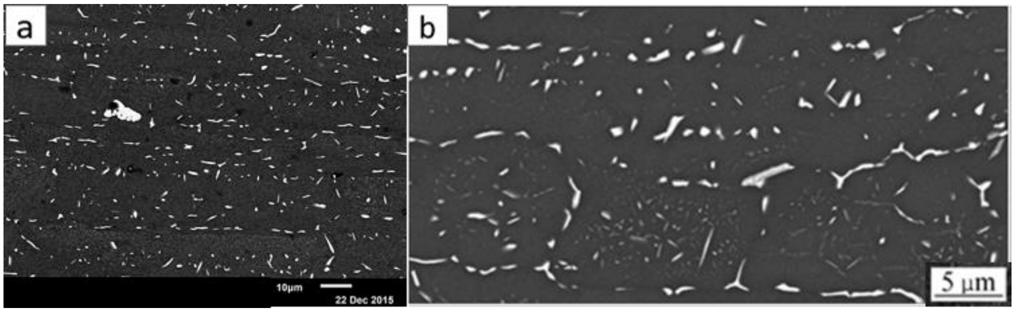

Figure 6-2: Through thickness LS plane SEM (a) AA7050-T6 (b) AA7150-T77 [41].

Conversely, the CDS material exhibited clustering of IMPs at triple points of grain boundaries as seen in Figure 6-3. IMP clusters consisted of Cu dominated S and θ IMPs. Often IMP clusters contained Fe-based IMPs and occasionally Ti IMP. Work previously done by Ghiaasiaan et al. [2] showed that in the as-cast condition the eutectic $Mg(Zn,Cu,Al)_2$ phase segregated to the grain boundaries (Figure 6-3b). T4 solutionizing heat treatment dissolved much of the eutectic phase, only reappearing entrapped inside bulky S ($CuMgAl_2$) phase. In the T4 condition much of the Fe was in bulky Cu_2FeAl_7 phase with some in the rod form. (Figure 6-3c,d) [2].

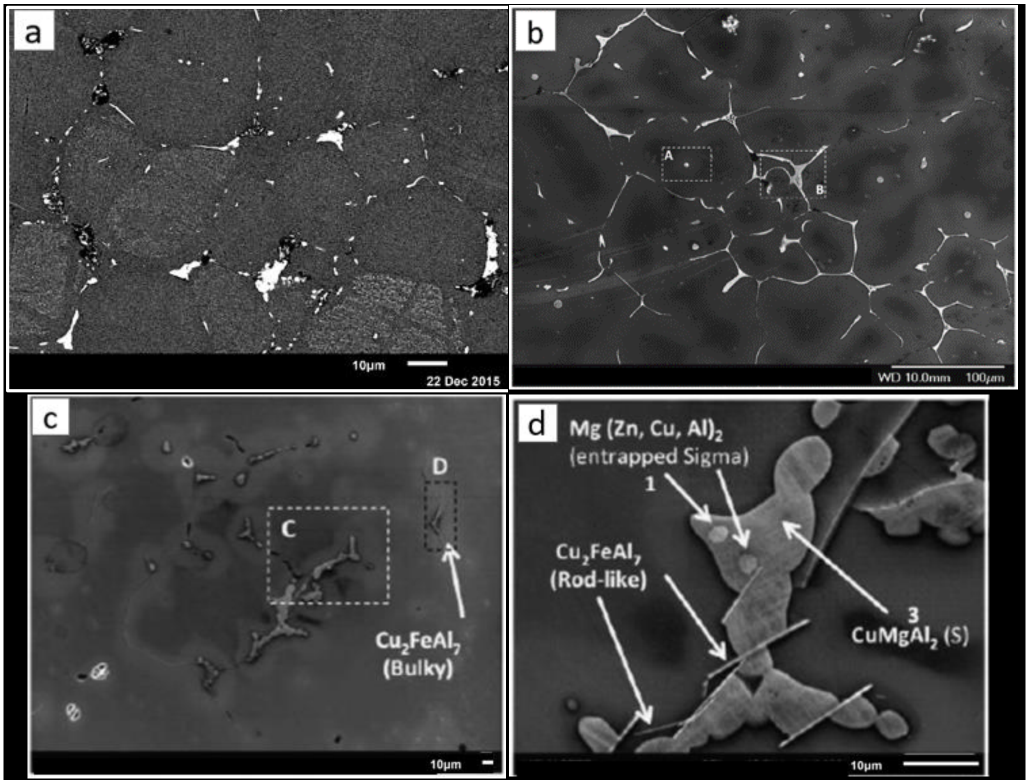

Figure 6-3: CDS IMPs: (a) CDS-T6 IMPs (b) CDS-as cast [2] (c),(d) CDS-T4. [2]

APT grain boundary reconstructions were clipped to remove the grain boundaries such that the η ($MgZn_2$) strengthening precipitate density could be measured by counting the number of η precipitates in the clipped volume. The wrought material had a precipitate density of 10.8×10^5 ppt/m^3, whereas the CDS material had a precipitate density of 8.15×10^5 ppt/m^3 (25% less). This could be due to the CDS material having a lower bulk Zn content (1%) and Mg (0.3%).

APT investigation of the grain boundary η precipitate revealed significant amounts of Cu in the precipitate which was previously speculated by Knight et al. [29]. A similar investigation was conducted by Wang et al. [42] on AA7055 in the T6 and T77 condition. Figure 6-4 compares the results of the CDS and wrought material with those observed by Wang et al.: It is seen the precipitates in the wrought and CDS were more distinct compared to those in Wang et al., with a stronger depletion of Al. The Zn/Mg ratio in the CDS material better matched those observed in Wang et al. But the Zn/Mg ratio in the wrought was inversed. It is unclear whether this is a feature of the wrought or not. One explanation may be preferential contamination by Ga bombardment during the FIB needle preparation process creating this as an artifact [35].

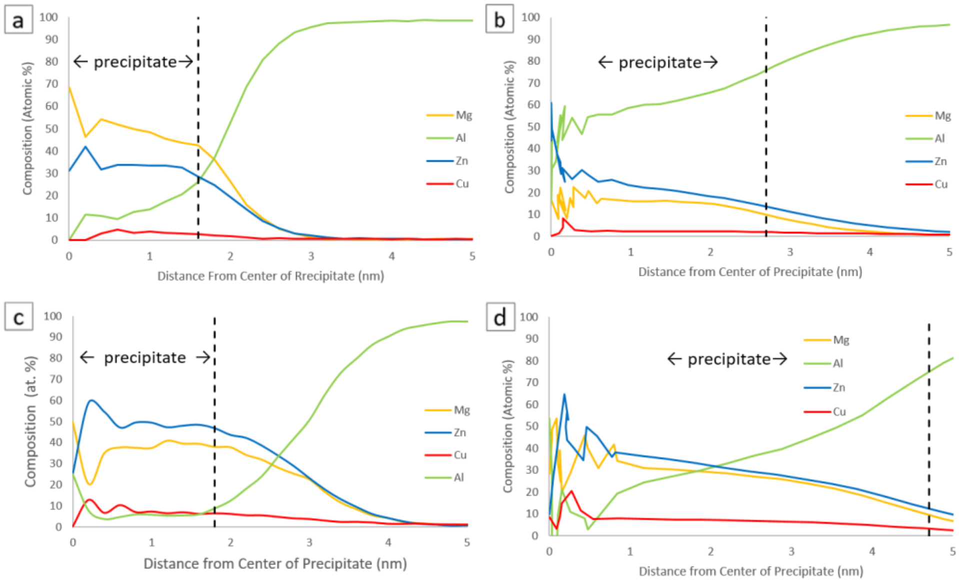

Figure 6-4: η grain boundary APT proxigrams (a) Wrought (b) Wrought AA7055-T6 [42] (c) CDS (b) Wrought AA7055-T73 [42]

A direct comparison of the Cu content in the measured η grain boundary precipitate was made below in Figure 6-5 between the wrought and the CDS material. It is seen the CDS material had as much as 3.5% more Cu segregated to the grain boundary precipitate than the wrought material: 5.2 ± 0.6 % Cu in the CDS versus 1.8 ± 0.4 % Cu in the wrought material. This difference in Cu content in the η precipitate, though, is not significant enough to play a major role in the overall IGC E_b [43].

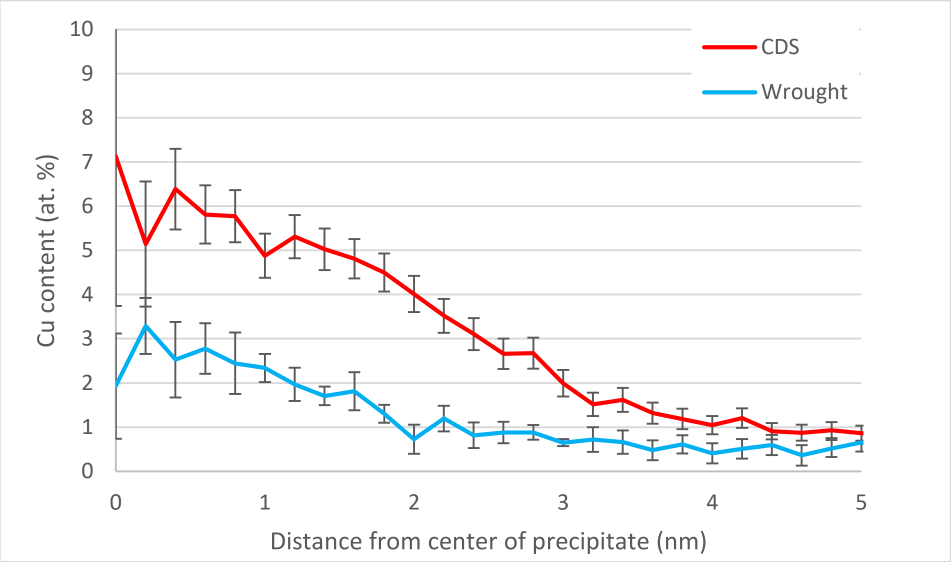

Figure 6-5: Comparison of Cu content in the η grain boundary precipitates of the Wrought and CDS material investigated via APT.

A comparison of the chemistry in the PFZ near the η precipitates was made by use of APT. The differences in the PFZ chemistry are shown in Table 6-4. The CDS material PFZ had higher amounts of Mg while the wrought material PFZ had higher amounts of Zn. Both PFZs are dominated by Al content. However, it is interesting to note that that in both PFZs there remains small amounts of Zn despite the constituent amount of Cu in both η precipitates.

Table 6-4: PFZ chemistry in wrought and CDS HAGB.

Material	**Zn%**	**Mg%**	**Cu%**	**Zn/Mg ratio PFZ**	**Zn/Mg ratio η precipitate**
Wrought	0.49 ± 0.06	0.82 ± 0.03	0.45 ± 0.04	0.6	0.66
CDS	0.28 ± 0.06	1.13 ± 0.03	0.41 ± 0.03	0.25	1.25

Though the CDS material exhibited less Cu-rich S/θ IMPs, the S/θ grain boundary precipitates themselves generally had a higher Cu content, with as much as 10% more Cu found in the CDS material than those found in the wrought material as revealed by AES. This difference was seen when comparing depth profiles of the wrought (Figure 5-12) vs. the CDS (Figure 5-24). This increase in Cu content increases the nobility of the precipitates with respect to the PFZ and matrix around them [15] [44]. This increase results in enhanced trenching during corrosion and dealloying of the IMP. This effect, combined with precipitate clustering increases the probability of stable pitting to initiate. A summary of the significant differences between the wrought and CDS material microstructures is shown in Table 6-5.

Table 6-5: Summary comparison of microstructural differences between wrought and CDS materials.

	Microstructure	
Grain Structure *GB Misorientation*	• Elongated grains • 60-80% HAGB	• Equiaxed grains • 50-70% HAGB
	Precipitates	
	Fe-Rich IMP	
Size Distribution	• Rarely of substantial size (<1) • Finely dispersed,	• Large (5-10 μm) • Trapped at triple points
	Grain Boundary η	
Mg/Zn ratio Cu content	• 1:1 • 2% Cu	• 3:2 • 5% Cu
	Grain Boundary S and θ	
Cu Content *Distribution*	• 40% Cu • Al,Zn,Mg • Redistributed by thermomechanical processing, aligned along grain boundaries	• 50% Cu • Al • Clusters at triple points, lower overall in count

6.2 *Differences in Corrosion Initiation*

Investigation of localized corrosion from short-term (30 min.) potentiostatic anodic polarization tests showed that corrosion of the CDS material initiated as pitting corrosion. The pitting was localized in nature, with much of the exposed surface and grain boundaries left in the pristine condition. This can be understood by considering the presence of secondary phase particle clustering and large Fe/Ti-rich IMPs in the CDS-processed material. These sites were generally found at the triple points of grain boundaries and make excellent sites where stable pitting can be initiated [44] [45]. Clustering of noble S and θ IMPs can lead to excessive trenching of the matrix and Cu dealloying. Large Fe/Ti-rich IMPs are very chemically active and are prone to extensive dealloying leading to the formation of stable pits [15] [44]. Potentiostatic testing showed that the pitting corrosion initiated at local locations leaving the majority of exposed grain boundaries unattacked even after extended testing.

Conversely, the wrought-processed material exhibited selective grain boundary attack (presumably grain boundaries with a high level of misorientation) with large areas left in the pristine condition. Since the wrought-processed material was thermo-mechanically processed, the large Fe-rich IMPs formed during the casting stage are broken down and redistributed to an inconsequential size as observed in SEM investigation (Figure 5-5a). The rolling process also results in redistribution of the S and θ phase IMPs making clustering less prevalent through the microstructure. This limits conditions suitable pitting and results in IGC dominating corrosion initiation.

6.3 *Differences in Corrosion Propagation*

In the CDS-processed material long-term (5 h) potentiostatic anodic polarization tests showed a transition from localized pitting to a mixed mode of localized pitting and grain exfoliation preceded by short range IGC, which initiated from the base of stable pits. During the test, both planes exposed exhibited pits that penetrated as deep as 200 μm while some pits penetrated only 50-100 μm, while some others areas remained in the pristine condition (Figure 5-29).This can be expected as once large Fe-rich IMPs and Cu-rich IMP clusters are consumed the driving force for further pitting decreases. This consumption allows for IGC to become more prominent. Local pit environments with low pH may increase the anodic potential of the exposed grain boundary further promoting IGC [46] [47].

The long-term exposure of the wrought-processed material on the LT plane showed that corrosion propagated by purely IGC to a max depth of 300 μm (Figure 5-27c). Exposure of LS and ST planes showed preferential grain boundary attack up to 600 μm along elongated grain boundaries in the traverse and rolling direction (Figure 5-28). In all exposed conditions potentiostatic anodic polarization resulted in little exfoliation corrosion.

When exposed to the cyclic salt fog conditions the CDS-processed material exhibited deep pitting that was preceded by short range IGC similar to that observed after long-term potentiostatic anodic polarization. The pits tended to be elliptical and with undercutting in shape and deep relative to the depth of general corrosion with a pitting factor of 5.8±1. Some pits exhibited grain etch-out with strong anisotropic characteristics Figure 5-33. The wrought-processed material suffered from classic exfoliation: corrosion exhibited wide, shallow trenches along the rolling direction preceded by short range IGC (Figure 5-29). The CDS-processed material had a 25% higher corrosion rate of 0.1890 ± 0.0653 mm/yr than the wrought-processed material of 0.151 ± 0.092 mm/yr over the duration of 30 weeks of testing. Pit analysis showed that the difference in mass loss could be explained by the high pitting factor in the CDS-processed material, while the wrought-processed material had very shallow trenching.

6.4 *Electrochemical behavior*

Potentiodynamic and potentiostatic polarization showed that the CDS-processed material exhibited a pitting corrosion E_b of -694±5 mV_{SCE}, which was 50 mV above the IGC E_b of -752±6 mV_{SCE} exhibited by the wrought-processed material as summarized in Table 6-6. OCP measurements of the fracture surfaces showed that the OCP of the wrought-processed material fracture surface was essentially the same as the IGC E_b as determined from the potentiodynamic anodic polarization measurement. While the OCP of the CDS-processed material fracture surface was 100 mV below its pitting corrosion E_b of -794 mV_{SCE}.

Table 6-6: Summary of comparison of corrosion and electrochemical behavior in wrought and CDS material.

Attribute	**Wrought**	**CDS**
Initiation	IGC	Localized Pitting
E_B	-752 mV_{SCE}	-694 mV_{SCE}
Propagation	IGC	Pitting + IGC
Grain Boundary OCP	- 747 mV_{SCE}	-794 mV_{SCE}

Cu segregation has a strong influence on the local electrochemical activity of precipitates and grain boundaries [12]. The SEM investigation of the wrought and CDS material revealed differences in the distribution of S and θ precipitates as seen when comparing some of the grain boundaries in Figure 6-6. Since CDS is a process designed to reduce segregation and the formation of secondary phases, it was expected that there were few S and θ precipitates at the grain boundaries relative to that of the wrought material.

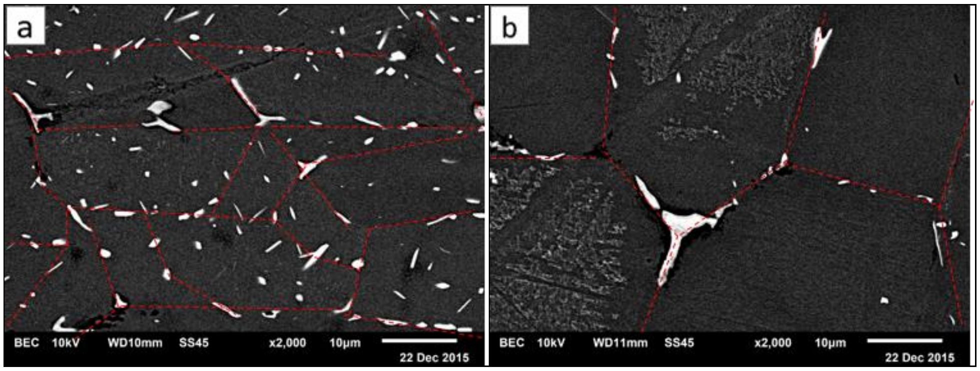

Figure 6-6: Comparison of IMP density of grain boundaries (a) Wrought LS plane (b) CDS L plane.

The fracture surface OCP is a measurement of the electrochemical activity of the grain boundary [29]. Fracture surfaces were compared with extensive studies of fracture modes done by Dumont et al. on AA7050 [48] [49] .as seen in Figure 6-7. Both material fracture surfaces fit the characterization of intergranular ductile fracture Figure 6-7a as evident of the lack of large dimples and abundance of grain boundary precipitates.

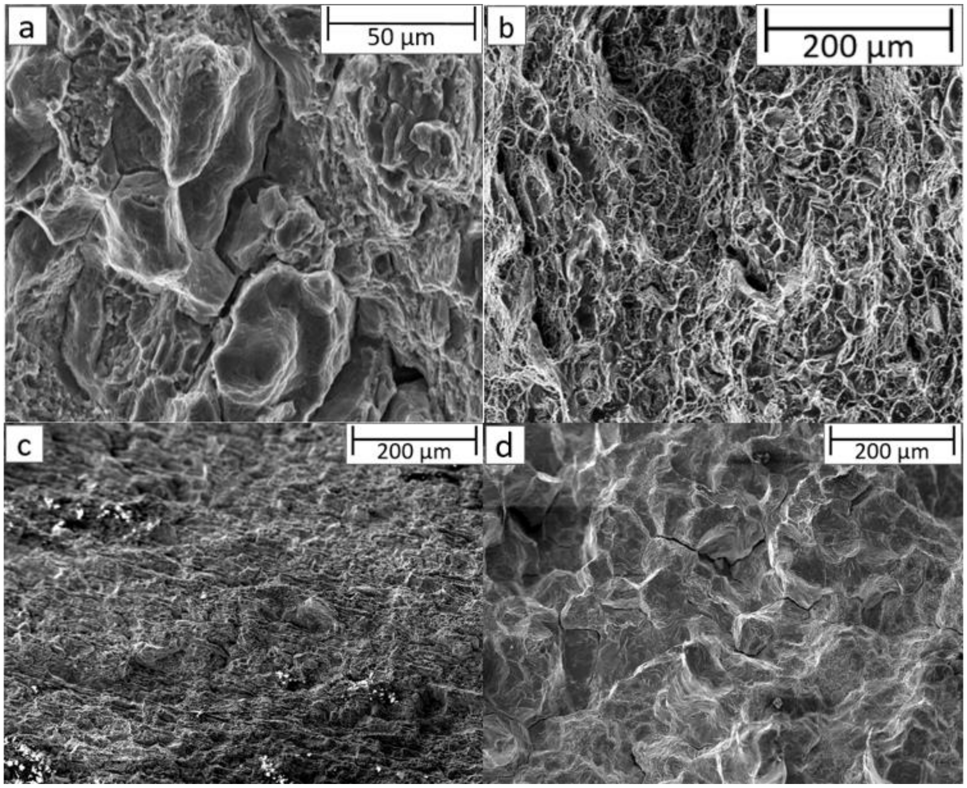

Figure 6-7: Fractures surfaces: (a) Intergranular ductile fracture [49]. (b) Intragranular ductile fracture [49]. (c) Wrought fracture (d) CDS fracture.

It is expected that the wrought fracture surface OCP to match its breakdown potential as localized corrosion was found to initiate and propagate as purely IGC in this material. The close match between these two confirms that intergranular fracture dominated the fracture surfaces. The OCP of the intergranular-dominated fracture surface showed that the CDS grain boundary was more anodic then the wrought grain boundaries, supporting the notion that fewer Cu-rich precipitates decorate the grain boundaries. This difference in the Cu-rich grain boundary precipitate count suggests that more of the Cu remains in solid solution (matrix) in the CDS material relative to the wrought material. This results in a solid solution matrix that is more noble reducing the pitting potential [42]. Despite having a more anodic grain boundary, the CDS material (as-polished surface) is initially susceptible to pitting corrosion. This could be a function of the OCP of the grain boundary relative to the matrix solid solution. Larger equiaxed grains could also be extending the diffusion length for IGC making pitting more feasible. This theory would need to be validated by comparing the effect of grain size on CDS susceptibility to IGC. Current transients from the potentiostatic anodic polarization testing (Figure 5-30) showed that the CDS material corroded at a significantly higher rate (anodic current density) relative to the wrought material. This difference in anodic current density transients needs to be interpreted with some care since the CDS material suffered from grain etch-out and pitting, both of which increase the exposed surface area enhancing the measured anodic current density.

Chapter 7: **Conclusions**

CDS is an innovative casting technique designed to enable the application of AA7050 for the use of thin wall casting. The CDS processing method results in a completely equiaxed granular microstructure that provides similar mechanical properties (hardness) as the wrought processing. Major conclusions extracted from this work includes the following:

1. The CDS-processed material resulted in granular structure unlike the wrought-processed material; it is susceptible to pitting corrosion rather than IGC. Due to the absence of thermo-mechanical processing, large Fe-rich IMPs and clusters of and S/θ particles remain in the microstructure, which initiates stable pitting corrosion. The CDS-processed material exhibited a reduced level of Cu segregation, which limited the formation of S/θ particles on the grain boundaries.
2. Corrosion of the equiaxed microstructure of the CDS-processed material results in large grain etch-out. This mode increases the mass loss and anodic current density transients but inhibits deep IGC. This corrosion mode allows much of the gauge thickness to remain intact after substantial corrosion.

3. The overall localized corrosion susceptibility of the CDS-processed material is similar to that of the wrought-processed material as evaluated using both accelerated testing (potentiostatic anodic polarization) and more realistic (cyclic acidified salt fog) testing, demonstrating that overall there isn’t a substantial increase in overall corrosion susceptibility.
4. The CDS material showed a higher sensitivity to Cu and impurity content. Although the CDS process resulted in fewer S/θ particles, the Cu content in them was higher resulting in IMP clusters which are more chemically active. Also, Fe impurities manifested themselves in IMP clusters and resulted in sites where stable pitting could be initiated. Impurity control, especially Fe, is crucial to preventing increased susceptibility.

References

[1] J. Hirsch, "Automotive Trends in Aluminium - The European Perspective," *Materials Forum,* vol. 28, no. (1), pp. 15-20, 2004.

[2] R. Ghiaasiaan, X. Zeng and S. Shankar, "Controlled Diffusion Solidification (CDS) of Al-Zn-Mg-Cu(7050): Microstructure,heat treatment and mechanical properties," *Materials Science & Engineering A,* no. 594, pp. 260-277, 2014.

[3] X. Fang, Y. Du, M. Song, K. Li and . C. Jiang, "Effects of Cu content on the precipitation process of Al–Zn–Mg alloys," *Journal of Materials Science,* no. 47, pp. 8174-8187, 2012.

[4] J. E. Hatch, Aluminum: Properties and Physical Metallurgy, ASM, Metals Park, OH, 1983.

[5] E. Lunarska, E. Trela and Z. Szklarska-Smialowska, "Pitting Corrosion of Powder Metallurgy AlZnMg Alloys," *Corrosion,* vol. 4, no. 43, pp. 219-228, 1987.

[6] N. Dimitrov, J. A. Mann, M. Vukmirovic and K. Sieradzki, "Dealloying of Al2CuMg in Alkaline Media," *Journal of The Elctrochemical Society,* vol. 9, no. 147, pp. 3283-3285, 2000.

[7] C. S. Paglia, K. V. Jata and R. G. Buchheit, "A cast 7050 friction stir weld with scandium: microstructure, corrosion and enviromental assisted cracking," *Materials Science and Engineering A,* vol. 424, no. 1-2, pp. 196-204, 2006.

[8] A. E. Hughes, N. Birbilis, J. M. Mol, S. J. Garcia, X. Zhou and G. E. Thompson, "High Strength Al-Alloys: Microstructure, Corrosion and Principles of Protection," in *Recent Trends in Processing and Degradation of Aluminium Alloys*, P. Z. Ahmad, Ed., InTech, 2011, pp. 223-262.

[9] E. Martínez-Flores and G. Torres-Villasenor, "Hibrid Materials Based on Zn-Al Alloys," in *Metal, Ceramic and Polymeric Composites for Various Uses*, J. Cuppoletti, Ed., InTech, 2011, pp. 149-170.

[10] M. Flemings, Solidification processing, Mcgraw-Hill College, 1974.

[11] X. Xu, E. Schlangen and S. van der Zwaag, "Linking Porosity to Rolling Reduction and Fatigue Lifetime of Hot

Rolled AA7xxx Alloys by 3D X-Ray Computed Tomography**," *Advanced Engineering Materials,* vol. 14, no. 7, pp. 457-463, 2012.

[12] Q. Meng and G. S. Frankel, "Effect of Cu content on Corrosion Behavior of 7xxx Series Aluminum Alloys," *Journal of the Electrochemical Society ,* vol. 151, no. 5, pp. B271-B283, 2004.

[13] E. McCafferty, "Sequence of steps in the pitting of aluminum by chloride ions," *Corrosion Science,* vol. 25, no. 2, pp. 1421-1438, 2003.

[14] G. S. Frankel, "Pitting corrosion of Metals: A Review of the Critical Factors," *Journal of The Electrochemical Society,* vol. 145, no. 6, pp. 2186-2186, 1997.

[15] G. O. Ilevbare, O. Schneider, R. G. Kelly and J. R. Scully, "In Situ Confocal Laser Scanning Microsopy of AA 2024-T3 Corrosion Metrology: I. Localized Corrosion of Particles," *Journal of The Electrochemical Society,* vol. 151, no. 8, pp. B453-B464, 2004.

[16] R. G. Buchheit, M. A. Martinez and L. P. Montes, "Evidence for Cu Ion Formation by Dissolution and Dealloyig the

Al2CuMg Intermetallic Compound in Rotating Ring-Disk Collection Experiments," *Journal of The Electrochemical Society,* vol. 147, no. 1, pp. 119-124, 2000.

[17] M. B. Vukmirovic, N. Dimitrov and K. Sieradzki, "Dealloying and Corrosion of Al Alloy 2024 T3," *Journal of The Electrochemical Society,* vol. 149, no. 9, pp. B428-B439, 2002.

[18] A. Boag, A. E. Hughes, A. M. Glenn, T. H. Muster and D. McCulloch, "Corrosion of AA2024-T3 Part I: Localised corrosion of isolated IM particles," *Corrosion Science,* vol. 53, no. 1, pp. 17-26, 2011.

[19] Z. F. G. S. Zhao, "The effect of temper on the first breakdown in AA7075," *Corrosion Science,* vol. 49, p. 3089–3111, 2007.

[20] Z. Zhao and G. Frankel, "On the first breakdown in AA7075-T6," *Corrosion Science,* pp. 3064-3088, 2007.

[21] A. M. Glenn, T. H. Muster, C. Luo, X. Zhou, G. E. Thompson, A. Boag and A. E. Hughes, "Corrosion of AA2024-

T3 Part III: Propagation," *Corrosion Science,* vol. 53, no. 1, pp. 40-50, 2011.

[22] D. A. Wadeson, X. Zhou, G. E. Thompson, P. Skeldon, L. Djapic Oosterkamp and G. Scamans, "Corrosion behaviour of friction stir welded AA7108 T79 aluminum alloy," *Corrosion Science,* vol. 48, no. 4, pp. 887-897, 2006.

[23] ASM International, Corrosion of Aluminum and Aluminum Aloys, J. R. Davis, Ed., ASM International, 1999.

[24] American Society for Metals, Metals Handbook Desk Edition, Metals Park, Ohio: ASM International, 1985.

[25] S. Mostafapoor, M. Emamy and M. Malekan, "Effect of Ti-B Grain Refiner on Microstructure and Mechanical Properties of a New Super High Strength Aluminum Al-Cu-Mg-Zn Cast Alloy," in *2015 International Conference on Chemical, Metallurgy and Environmental Engineering*, Istanbul , 2015.

[26] ASTM E384-11e1, "Standard Test Method for Knoop and Vickers Hardness of Materials," ASTM International, West Conshohocken, 2011.

[27] B. Gault, M. P. Moody, J. M. Cairney and S. P. Ringer, Atom Probe Microscopy, New York: Springer New York Heidelberg Dordrecht London, 2012.

[28] ASTM E23-12c, "Standard Test Methods for Notched Bar Impact Testing of Metallic Materials," ASTM International, West Conshohocken, 2012.

[29] S. P. Knight, N. Birbilis, B. C. Muddle, A. R. Trueman and S. P. Lynch, "Correlations between intergranular stress corrosion cracking, grain boundary microchemistry, and grain-boundary electrochemistry for Al-Zn-Mg-Cu alloys," *Corrosion Science,* no. 52, pp. 4073-4080, 2010.

[30] International, ASTM, ASTM B117-16, Standard Practice for Operating Salt Spray (Fog) Apparatus, West Conshohocken, PA,, 2016.

[31] ASTM International, ASTM G85-11, Standard Practice for Modified Salt Spray (Fog) Testing, West Conshohocken, PA, 2011.

[32] ASTM International, ASTM G1-03(2011), Standard Practice for Preparing, Cleaning, and Evaluating Corrosion Test Specimens, West Conshohocken, PA, 2011.

[33] D. A. Jones, Principles and Prevention of Corrosion, Upper Saddle River, NJ: Prentice-Hall, 1996.

[34] "Properties and Selection Nonferrous Alloys and Special-Purpose Materials," in *Metals Handbook*, 10th ed., vol. 2, ASM International, 1990.

[35] B. Langelier, Interviewee, *Personal Communications.* [Interview]. 23rd Febuary 2015.

[36] S. P. Knight, M. Salagaras and A. R. Trueman, "The study of intergranular corrosion in aircraft aluminum alloys using X-ray tomography," *Corrosion Science,* vol. 53, no. 2, pp. 727-734, 2011.

[37] T. J. Turner and M. P. Miller, "Modeling the Influence of Material Structure of Defornation Induced Surface Roughening in AA7050 Thick Plate," *Journal of Engineering Materials and Technology,* vol. 129, no. 3, pp. 367-379, 2005.

[38] R. Ghiassiaan, S. Shankar and D. Apelian, Control Diffusion Solidification (CDS): An Overview of Mechanism and Application, J. C. a. G. B. M. Tiryakioğlu, Ed., Hoboken, NJ,: M. Tiryakioğlu, J. Campbell and G. Byczynski, 2014.

[39] W. Gu, J.-y. Li and Y.-d. Wang, "Effect of dislocation structure evolution on low-angle grain boundary formation in 7050 aluminum alloy during aging," *International Journal of Minerals, Metallurgy and Materials ,* vol. 22, no. 7, pp. 721-728, 2015.

[40] T. Minoda and H. Yoshida, "Effect of grain boundary characteristics on the intergranular corrosion resistance of 6061 aluminum alloy extrusion," *Metallurgical and Materials Transactions A,* vol. 33, no. 9, pp. 2891-2898, 2002.

[41] P. Rometsch, Y. Zhang and S. Knight, "Heat treatment of 7xxx series aluminium alloys—Some recent developments," *Transactions of Nonferrous Metals Society of China,* vol. 24, no. 1, pp. 2003-2017, 2017.

[42] S.-S. Wang, I.-W. Huang, L. Yang, J.-T. Jiang, J.-F. Chen, S.-L. Dai, D. Seidman, G. S. Frankel and L. Zhen, "Effect of Cu Content and Aging Conditions on Pitting Corrosion

Damage of 7xxx Series Aluminum Alloys," *Journal of The Electrochemical Society,* vol. 162, no. 4, pp. 150-160, 2015.

[43] T. Ramgopal, P. Schmutz and G. S. Frankel, "Electrochemical Behavior of Thin Film Analogs of Mg(Zn,Cu,Al)2," *Journal of The Elctrochemical Society ,* vol. (9), p. 148, 2001.

[44] C. M. Liao, J. M. Olive, M. Gao and R. P. Wei, "In-Situ Monitoring of Pitting Corrosion in Aluminum Alloy 2024," *Corrosion Science,* vol. 54, no. 6, pp. 451-458, 1996.

[45] A. Boag, R. J. Taylor, T. H. Muster, N. Goodman, D. McCulloh, C. Ryan, B. Rout and D. Jamieson, "Stable pit formation on AA2024-T3 in a NaCl environment," *Corrosion Science,* vol. 52, no. 1, pp. 90-103, 2010.

[46] T. D. Burleigh, E. Ludwiczak and R. A. Petri, "Intergranular Corrosion of an Aluminum-Magnesium-Silicon-Copper Alloy," *Corrosion Science,* vol. 51, no. 1, pp. 50-55, 1995.

[47] V. Guillaumin and G. Mankowski, "Localized corrosion of 6056 T6 aluminium alloy in chloride media," *Corrosion Science,* vol. 42, no. 1, pp. 105-125, 2000.

[48] T. Pardoen, D. Dumont, A. Deschamps and Y. Brechet, "Grain boundary versus transgranular ductile failure," *Journal of the mechanics and physics of solids,* vol. 51, no. 1, pp. 637-665, 2003.

[49] D. Dumont, A. Deschamps and Y. Brechet, "On the relationship between microstructure, strength and toughness in AA7050 aluminum alloy," *Materials Science and Engineering A,* vol. 356, no. 1, pp. 326-336, 2003.

[50] D. A. Jones, Principles and Prevention of Corrosion, Upper Saddle River, NJ: Prentice-Hall, 1996.

[51] ASTM G46-94(2013), " Standard Guide for Examination and Evaluation of Pitting Corrosion," ASTM International, West Conshohocken, PA, 2013, DOI: 10.1520/G0046, www.astm.org.

[52] G. O. Ilevbare, O. Schneider, R. G. Kelly and J. R. Scully, "In Situ Confocal Laser Scanning Microscopy of AA 2024-T3 Corrosion Metrology," *Journal of The Electrochemical Society,* vol. 151, no. 8, pp. 453-464, 2004.